Icarus **149**, 133–159 (2001)
doi:10.1006/icar.2000.6498, available online at http://www.idealibrary.com on IDEAL®

Energetic Ion and Electron Irradiation of the Icy Galilean Satellites

John F. Cooper

Raytheon Information Technology and Scientific Services (ITSS), SSDOO Project, Code 632, NASA Goddard Space Flight Center, Greenbelt, Maryland 20771
E-mail: jfcooper@pop600.gsfc.nasa.gov

Robert E. Johnson

Engineering Physics, Thornton Hall B103, University of Virginia, Charlottesville, Virginia 22903, and NASA/Goddard Institute for Space Studies, 2880 Broadway, New York, New York 10025

Barry H. Mauk

Applied Physics Laboratory/Johns Hopkins University, 11100 Johns Hopkins Road, Laurel, Maryland 20723-6099

Henry B. Garrett

Jet Propulsion Laboratory, M/S: 301-456, 4800 Oak Grove Drive, Pasadena, California 91109-8099

and

Neil Gehrels

Laboratory for High Energy Astrophysics, Code 661, NASA Goddard Space Flight Center, Greenbelt, Maryland 20771

Received October 26, 1999; revised May 15, 2000

Galileo Orbiter measurements of energetic ions (20 keV to 100 MeV) and electrons (20–700 keV) in Jupiter's magnetosphere are used, in conjunction with the JPL electron model (<40 MeV), to compute irradiation effects in the surface layers of Europa, Ganymede, and Callisto. Significant elemental modifications are produced on unshielded surfaces to approximately centimeter depths in times of $\leq 10^6$ years, whereas micrometer depths on Europa are fully processed in ~10 years. Most observations of surface composition are limited to optical depths of ~1 mm, which are in direct contact with the space environment. Incident flux modeling includes Størmer deflection by the Ganymede dipole magnetic field, likely variable over that satellite's irradiation history. Delivered energy flux of $\sim 8 \times 10^{10}$ keV (cm^2-s)$^{-1}$ at Europa is comparable to total internal heat flux in the same units from tidal and radiogenic sources, while exceeding that for solar UV energies (>6 eV) relevant to ice chemistry. Particle energy fluxes to Ganymede's equator and Callisto are similar at ~ 2–3×10^8 keV (cm^2-s)$^{-1}$ with 5×10^9 at Ganymede's polar cap, the latter being comparable to radiogenic energy input. Rates of change in optical reflectance and molecular composition on Europa, and on Ganymede's polar cap, are strongly driven by energy from irradiation, even in relatively young regions. Irradiation of nonice materials can produce SO_2 and CO_2, detected on Callisto and Europa, and simple to complex hydrocarbons. Iogenic neutral atoms and meteoroids deliver negligible energy $\sim 10^{4-5}$ keV (cm^2-s)$^{-1}$ but impacts of the latter are important for burial or removal of irradiation products. Downward transport of radiation produced oxidants and hydrocarbons could deliver significant chemical energy into the satellite interiors for astrobiological evolution in putative sub-surface oceans. © 2001 Academic Press

Key Words: **radiation chemistry; surfaces, satellite; Europa; Ganymede; Callisto.**

1. INTRODUCTION

Chemical composition and evolution of surface ices on Europa, Ganymede, and Callisto are of great interest for understanding the satellites' origin, exterior atmospheres, and interactions with the jovian magnetosphere. For Europa a primary interest is the existence of a subsurface ocean (Squyres *et al.* 1983) suggested by Galileo Orbiter imaging of disrupted terrain (Belton *et al.* 1996, Carr *et al.* 1998, Sullivan *et al.* 1998, Williams and Greeley 1998). Hydrated minerals, perhaps from ocean salts in Europan terrain fractured by tidal stresses, may account for spectral absorption features in near-IR reflectance spectra obtained by Galileo (McCord *et al.* 1997, 1998a,b, 1999). Current models for Galileo Orbiter measurements of the Europa and Callisto magnetic field environments include internal current induction in the liquid water layer of each satellite (Khurana *et al.* 1998, Kivelson *et al.* 1999) by time-varying components of external magnetic fields from the jovian magnetosphere (Khurana 1997).

0019-1035/01 $35.00

The ages of the satellite surfaces have been estimated from impact crater statistics and limit the combined cumulative effects of impacts, irradiation, and crustal instabilities on these time scales. A current estimate of minimum surface age for Europa from cratering is 10^7 years, as compared to 4×10^9 years for Callisto and $0.5–1.0 \times 10^9$ years for Ganymede (Zahnle *et al.* 1998). Neukum (1997) alternatively advocates a large range of ages up to 10^9 years for Europa's surface with an average of $\sim 10^8$ years. Models for internally driven resurfacing of Ganymede over 10^7 to 10^8 years have been proposed (Showman and Malhotra 1997, Showman *et al.* 1997, Shoemaker and Wolfe 1982). Rising diapirs (plumes of low viscosity ice) from solid state convection (Pappalardo *et al.* 1998) are common features in mottled terrain covering much of the Europan surface (Carr *et al.* 1998). Such terrain might arise from localized thermal runaway (McKinnon 1999, Carr *et al.* 1998, Spaun *et al.* 1998).

The satellite surfaces are also modified chemically and eroded by irradiation from magnetospheric particles, UV photons, energetic neutral atoms (ENAs) from the Io torus, and meteoritic bombardment. Results reported here indicate that timescales for magnetospheric ion and electron effects are as short as a few years at micrometer depths and less than a few million years within the thin optical layer of ≤ 1 cm accessible to remote sensing observations. The energetic particle and UV effects are shown to be competitive at sub-micrometer depths but the more penetrating particles dominate chemical processing in most of the optical layer. For many chemical reactions of interest, e.g., H_2O dissociation, the UV energy fluxes above the relevant threshold energies of ≥ 6 eV are relatively insignificant as compared to the particle energy fluxes (Section 6). Micrometeoroid bombardment produces the main jovian rings by impacts on small satellites (Ockert-Bell *et al.* 1998, Burns *et al.* 1999) and the newly discovered rings around larger satellites by impacts on surfaces of those satellites (Krüger *et al.* 1999). Although the energy deposition for chemical change from micrometeoroids and ENAs is found here to be insignificant compared to particle and UV effects, the micrometeoroids may play a crucial role in burial of irradiation products beneath the impact ejecta and in vertically distributing these products below the optical layer through surface gardening effects (Section 6).

New *in situ* measurements of magnetospheric plasma, energetic particles, and micrometeoroids have now been acquired near each satellite during multiple encounters by the Galileo Orbiter spacecraft. The goal of the present work is to specify the incident energy fluxes and direct irradiation effects of energetic ions and electrons in the magnetospheric radiation environments near Europa, Ganymede, and Callisto. We include flux spectra for irradiation modeling only from the respective Galileo orbits G2, C3, and E4 (Sections 2 and 3); details of spatial and temporal variability for later measurements will be addressed in future work. Calculated irradiation effects dependent on penetration depth include electronic ionization from ion and electron energy losses, implantation of stopping particles, and local erosion by ion sputtering (Sections 5 and 6). Ip *et al.* (1997, 1998) and Paranicus *et al.* (1999) have used spectra for ions at Europa and Ganymede to calculate surface erosion rates due to ion sputtering; these results have been checked against our calculations. For Ganymede we calculate the effect of the magnetic field on irradiation parameters in the equatorial region (Section 4), while the full measured ion and electron spectra are found to apply to the polar cap region above 30° N/S satellite latitude.

Following a description of the chemistry induced by ion implantation (Section 7) and irradiation (Section 8) the above results are used to discuss irradiation-induced chemical evolution of the icy surfaces for nonice materials (Section 9). Some of the materials observed recently may be direct products of irradiation, such as H_2O_2 and hydrated H_2SO_4 on Europa, O_2 and O_3 on Ganymede, and CO_2 on Callisto. The constituent components of hydrated minerals are likely endogenic, but the molecular configurations of all materials in the optical layer may be the result of chemical reactions driven by the energy flux from magnetospheric plasma. Many laboratory experiments since Miller–Urey (Miller 1953) have demonstrated both the decomposition (Section 9.3) of mixed ices and minerals by irradiation, and the synthesis of simple to complex hydrocarbons (Section 9.4). In Section 10 we summarize our present results (Section 10.1) and further discuss issues such as the state of energetic particle measurements and models (Section 10.2), applications to interpretation of remote sensing data (Section 10.3), and potential impact of irradiation on astrobiological evolution for Europa and similar bodies in planetary systems elsewhere (Section 10.4).

2. ENERGETIC PARTICLE MEASUREMENTS

2.1. Galileo EPD Instrumentation and Data

The completed primary tour of the Jupiter system by the Galileo Orbiter, and the Galileo Europa Mission (GEM), are providing a wealth of energetic ion measurements from which accurate models of radiation environments for the Galilean satellites can be constructed. In this work we use energetic ion and electron flux spectra as measured by the Energetic Particle Detector (EPD) experiment (Williams *et al.* 1992). EPD data provide much improved elemental discrimination and extend the spectra to lower energies than covered by the comparable Low Energy Charged Particle (LECP) experiments (Krimigis *et al.* 1977) for the 1979 Voyager 1 and 2 encounters.

The EPD experiment includes two major subsystems, the Composition Measurement System (CMS) and the Low Energy Magnetospheric Measurement System (LEMMS). CMS uses a combination of $\mathrm{d}E(\mathrm{d}x)^{-1}$ vs E, total E, and time-of-flight (TOF) measurements to determine heavy ion ($Z > 1$) composition at total energies of 10 keV to 100 MeV. LEMMS provides data on total ion ($Z \geq 1$) intensity in the range of 20 keV to 55 MeV, which can be combined with CMS data to separate the ion spectra for H, O, and S in the Galilean satellite region of the jovian magnetosphere. The time-of-flight versus energy (TOF vs E) measurements from the CMS uniquely resolve the elemental

species H, O, and S. The EPD measurements do not, however, provide any direct information on the ion charge states, here assumed to be low, as discussed in the next section.

This work utilizes selected EPD ion spectra for Europa and Ganymede similar to those already published by Ip *et al.* (1997, 1998), while also including a new ion spectrum for Callisto and electron spectra for all three satellites. Figures 1, 2, and 3 show the ion and electron flux spectra acquired near the orbits of each satellite. The sampling times and locations in Table I were chosen for Europa and Ganymede to avoid the region of direct satellite sweeping for representation of the upstream environment near each satellite. The minimum averaging intervals were about 20 s, the spacecraft spin period. For Callisto the 5-h averaging interval was used to represent the time-averaged intensity as Callisto moved above and below the jovian plasma sheet (Section 2.2).

The ion flux spectra have been derived from fits of kappa distributions consisting of maxwellian thermal cores at lower energies and power-law tails at higher energies (Vasyliunas 1971, Divine and Garrett 1983, Kane *et al.* 1995, Mauk *et al.* 1996). The LEMMS channel data are fit using sums of the distributions for three ion species, H^+, O^{n+}, and S^{n+} ($n+$ refers to the unmeasured charge states) while the TOF vs E data from CMS are fit for each principal ion in the applicable energy ranges. All EPD spectral fits are weighted according to known energy thresholds and geometric factors for the ion and electron channels (Williams *et al.* 1992). EPD energy thresholds of spectra for e^-, H^+, O^{n+}, and S^{n+} are 21–23, 22, 45, and 82 keV, respectively, in total energy. Maximum energies are 121 MeV for ions and 682 keV for e^-. Here the O^{n+} and S^{n+} fluxes at the threshold

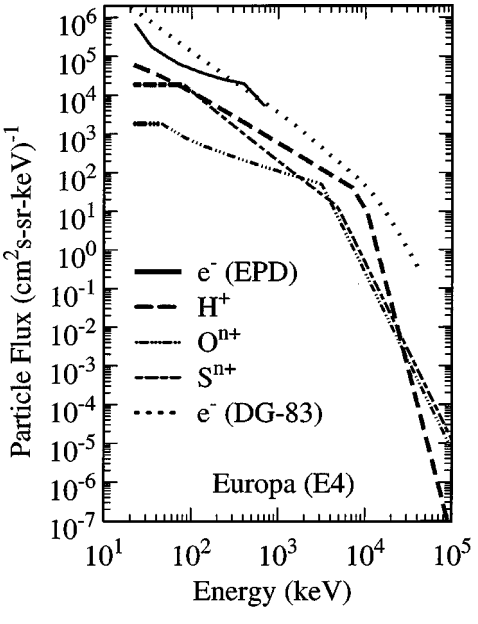

FIG. 1. Particle flux spectra from EPD measurements of the magnetospheric environment of Europa during the Galileo Orbiter's E4 encounter as functions of total particle energy for the sampling times and locations specified in Table I. The electron spectra are shown both from EPD at 20–700 keV and from the model spectrum (DG-83) of Divine and Garrett (1983) extending up to 40 MeV. The model electron spectrum, and the EPD ion spectra, are used for dosage calculations.

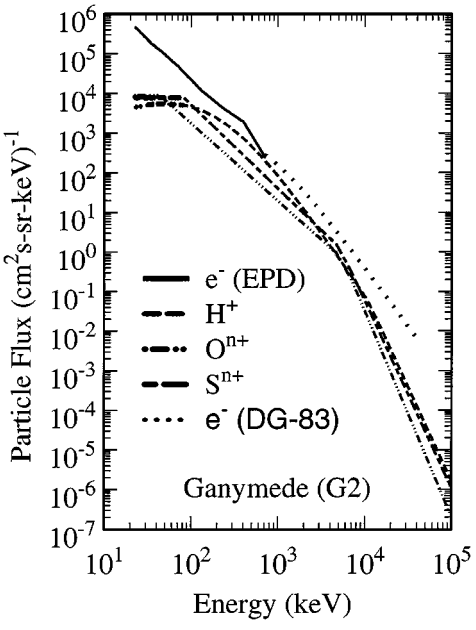

FIG. 2. Flux spectra representing the energetic particle environment upstream of Ganymede from EPD measurements during the Galileo Orbiter's G2 encounter and from DG-83, the Divine and Garrett (1983) model for electrons. Details are as given in Fig. 1 and in Table I, except that the model spectrum for electrons is used for dosage calculations only above 700 keV.

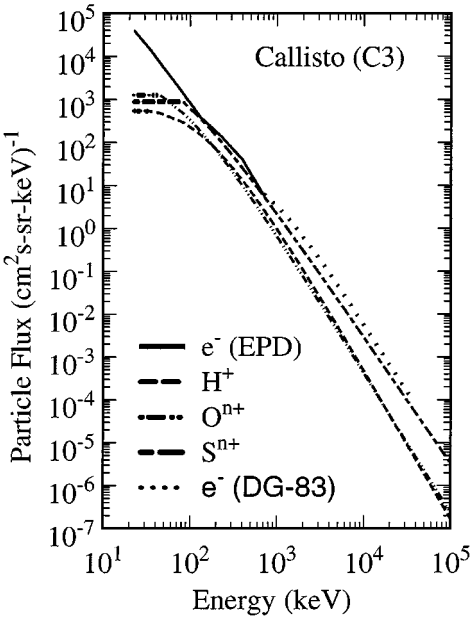

FIG. 3. Flux spectra for the energetic particle environment of Callisto from the Galileo Orbiter's C3 encounter and from DG-83, the Divine and Garrett (1983) model for electrons. Details are as already given in Fig. 2 and Table I.

TABLE I
Galileo Orbiter Ephemeris Parameters for EPD Flux Measurements

Satellite	Orbit	Date (SCET-UT)	Time (SCET-UT)	Jovicentric (System III, 1965)				Satellite-centered		
				r_J	λ_J (°)	φ_J (°)	λ_M (°)	r_S	λ_S (°)	φ_S (°)
Europa	E4	Dec. 19, 1996	06:40	9.40	−0.22	150.2	+5.70	3.13	−0.86	27.39
Ganymede	G2	Sept. 6, 1996	18:40	15.13	+0.13	147.0	+5.62	3.60	+11.67	168.78
Callisto	C3	Nov. 4, 1996	11:00	27.2	−0.18	151.4	+5.90	—	—	—
			16:00	25.3	−0.17	329.0	−5.94	—	—	—

Note. Radial distances are listed in units of either jovian ($R_J = 71{,}492$ km) or satellite (R_s) equatorial radii. The latter radii are defined here as 1560 km for Europa, 2634 km for Ganymede, and 2409 km for Callisto, as per documentation from the Planetary Plasma Interactions node of the Planetary Data System. Close approach times on the respective encounter days were approximately 06:52:58, 18:59:34, and 13:34:28 SCET-UT for E4, G2, and C3. Longitudes (φ) are given in the conventional senses, west from the prime meridian for jovicentric System III and east from the $+X_s$ axis directed toward Jupiter for "planetographic" satellite-centered positions. Latitudes (λ) are defined relative to the jovian and satellite equators, except that λ_M is jovimagnetic latitude relative to the dipole equator of Jupiter's planetary magnetic field. The E4 and G2 samples were taken, respectively, inbound to Europa at $2.8R_s$ in the $+X_s$ direction and outbound from Ganymede at $3.5R_s$ in the $-X_s$ direction. All three samples were therefore well outside the satellite "magnetospheres" of radial extent $r_s \lesssim 2R_s$. The jovian plasma sheet of vertical thickness $\sim 5R_J$ is approximately centered on the jovian dipole equator within the orbit of Callisto, so the E4 and G2 measurements occurred well within this region of hot iogenic plasma. The time-averaged C3 sample was taken at various positions up to $\sim 2R_J$ above the plasma sheet.

energies are extended as constants down to 22 keV for numerical calculations.

The EPD electron spectra used for each satellite are determined from power-law fits to LEMMS count rate channels; currently the EPD spectra extend only to 0.7 MeV but may be extended in later work. At higher energies we add extended spectra to 40 MeV from the JPL-supported model of Divine and Garrett (1983) as derived from Pioneer and Voyager measurements. The model fluxes are adjusted to match the 0.7-MeV endpoint from EPD.

The absolute fluxes of the EPD and model spectra agree within a factor of two or better at this energy but increasingly diverge by up an order of magnitude at lower energies down to 20 keV. The largest differences occur for the Callisto spectra and are likely due to spatial and temporal differences (Section 2.2) between measurements made at least 20 years earlier for the model and those from EPD in the current epoch. Higher particle intensities near and within the orbit of Ganymede can also cause count rate saturation in EPD electron channels below 300 keV. This instrumental problem mostly accounts for the EPD vs model differences in the low-energy Europa spectra of Fig. 1 and similarly affects Ganymede EPD data at times when intensities are higher than in the Fig. 2 spectra for the G2 orbit. The latter appears representative of time-average intensities from our samples of spectra during later orbits of the Galileo mission. For Europa the model spectrum in Fig. 1 best represents a corrected version of the EPD fluxes below 0.7 MeV, and the mixed EPD + model spectra are used for the other two satellites.

2.2. Spatial and Temporal Variability

In order to estimate time-averaged incidence of magnetospheric particle fluxes on the surface of each satellite, we consider variations with measurement location and measurement in the highly dynamic jovian magnetospheric environment. Time-scales for production of significant irradiation effects are many orders of magnitude greater than orbital periods of the satellites or our sampling intervals for accumulation of the EPD spectra. A particular source of spatial variation is the jovian plasma sheet, where plasma and energetic particle densities peak within an equatorial region of about five R_J in vertical thickness. The plasma sheet is roughly coplanar with the magnetic equatorial plane of Jupiter out to $30R_J$, so Callisto moves in and out of this region during the 10-h period of Jupiter's planetary rotation. The orbits of Europa and Ganymede lie entirely or mostly within the vertical extent of the plasma sheet, so spatial variations in incident particle intensity are less significant. However, temporal variability of hot plasma has been reported (Mauk *et al.* 1997, 1999) from EPD measurements between the orbits of Europa and Callisto. Samples from many crossings of the satellite orbits, including those from the ongoing Galileo Europa Mission may eventually change aspects of the modeling. However, we have already compared spectral fits for the Europa and Ganymede data used in this study to longer time averages of several hours and found no significant differences within the errors of the fits for selected energy ranges.

The question of temporal variation might be addressed from differences over 20 years between the EPD and LECP particle energy fluxes, but it is difficult to separate out the spatial and temporal differences. Mauk *et al.* (1996) reported the radial variation at 5 to $20R_J$ of ion and electron energy fluxes measured by LECP at crossings of the plasma sheet, where maximal trapped particle fluxes are expected along the local magnetic field line. Depending on whether the $Z \geq 1$ LECP channel responded to H^+ or heavy ions (e.g., O^+), the ion energy fluxes (assumed to be isotropic) in keV $(cm^2\text{-}s)^{-1}$ units were 1.4×10^{10} (H^+ or O^{n+}) near the orbit of Europa and 3.9×10^9 for H^+ (or 5.9×10^9 for O^{n+}) for Ganymede's orbit. Electron energy fluxes from LECP were 7.9×10^{10} keV $(cm^2\text{-}s)^{-1}$ for Europa and 3.9×10^{10} for Ganymede. Eyeball extrapolation of Fig. 3 in Mauk *et al.* (1996)

suggests an order of magnitude drop from 15 to $\sim 26 R_J$ for ions and electrons. Comparing these values to the EPD energy fluxes (cf., Section 5.1 and Table II), we see that the differences from the LECP equatorial values above for ions are minimal for Europa's orbit but progressively increase outward as expected for a latitudinal variation. The EPD electron energy fluxes decline outward in a similar manner. We find the number fluxes (not shown here) for >500 keV electrons near Europa's orbit to be similar to earlier measurements from the Voyager LECP experiments.

Therefore, the EPD ion and electron differences from Voyager measurements appear to be more spatial than temporal for the limited sample of EPD spectra presented here. We note, however, that the first Voyager LECP measurements at Jupiter (Krimigis *et al.* 1979) showed order of magnitude temporal variations even between the inbound and outbound passes of Voyager 1 at Callisto's orbit. As noted above, signatures of magnetospheric activity appear in EPD data throughout the Europa to Callisto region.

2.3. Charge States of Heavy Ions

In situ charge state measurements have been made in units of energy per ion charge by the Voyager Plasma Science (PLS) instruments to 6 keV e^{-1} (Bridge *et al.* 1979), by the Ulysses Solar Wind Ion Composition Spectrometer (SWICS) (Geiss *et al.* 1992) to 60 keV e^{-1}, and by the Galileo Plasma Spectrometer (PLS) experiment to 50 keV e^{-1} (Crary *et al.* 1998). Although the Voyager PLS data showed predominance of O^+ and S^+ states in the Io torus, the nonthermal (keV) plasma ions sampled further out near the orbit of Callisto included a significant S^{3+} component.

While the Voyager PLS data derived from electrostatic deflection were limited to energy per charge spectra and provided no discrimination between O^+ and S^{2+}, the Ulysses SWICS and Galileo PLS instruments used additional parameters. SWICS data added $dE(dx)^{-1}$ energy loss and time-of-flight parameters in triple coincidence mode (Geiss *et al.* 1992). The Galileo PLS used corotational anisotropy (i.e., S^{2+} varies more with look direction than O^+) for compositional separation. The SWICS data were, however, much less sensitive to singly charged ions, particularly S^+, while Crary *et al.* (1998) reported only on the 1+ and 2+ charge states. For $Q > 1+$ ions Geiss *et al.* (1992) found that O^{2+} and S^{3+} were dominant for Ulysses measurements mostly outside Europa's orbit, inbound to Jupiter, and outside Ganymede's orbit, outbound.

Hamilton *et al.* (1981) found that energetic ion spectra from the Voyager LECP instrument were well organized by energy per charge up to 20 MeV e^{-1} only for low charge states (e.g., O^{2+}–O^{3+}, S^{3+}–S^{4+}) of O and S atoms presumably originating from Io, and for high charge states (H^+, He^{2+}, H_3^+, C^{6+}, Fe^{12+}) of other ions more likely from the jovian ionosphere and the solar wind outside the magnetosphere. Collier and Hamilton (1995) later confirmed that the SWICS mean charge states of O^{2+} and S^{3+} provided excellent organization of the Voyager 2 LECP data in energy per charge units over 12 decades in phase space density for jovian plasma sheet crossings at 26–31 R_J. Keppler and Krupp (1996) used a similar approach with data from the Energetic Particle Composition (EPAC) experiment on Ulysses and also found a predominance of O^{2+} and S^{3+} in the keV to MeV iogenic ions. The present work assumes these latter values.

3. INCIDENT PARTICLE FLUX AND SATELLITE SWEEPING EFFECTS

3.1. Flux at the Satellite Surface

The measured flux spectra discussed above pertain to the energetic particles in the jovian magnetospheric environments outside the "mini-magnetosphere" of each satellite. Since we have ignored any pitch angle anisotropy by using spin-averaged flux spectra from the Galileo EPD experiment, it is first assumed here that an isotropic particle flux falls everywhere onto each surface. We ignore local magnetic field perturbations and previous sweeping of the trapped particle environments at the orbits of each satellite. The latter would otherwise deplete the downstream environment relative to the direction of plasma corotation. The integral omnidirectional flux F (cm^2-s)$^{-1}$ incident at any surface point is then just πJ, where J corresponds to the integrals of the spin-averaged flux spectra from EPD in Figs. 1–3 and the average incidence angle from the vertical (local zenith) is $Z_e \sim 45^\circ$ for a flat solid surface and incidence angle range $0^\circ < Z_e < 90^\circ$.

3.2. Corotation Effect

The isotropic assumption works well for more energetic (MeV) particles but breaks down at lower energies. The impact velocity for incidence of fresh pickup ions (neutral atoms ionized by solar UV or charge exchange interactions and then forced into corotation by the magnetic field) onto the trailing hemisphere is $v_i \leq 2(v_c - v_k)$ for full corotation velocity v_c within the planetary magnetic field and for satellite orbital velocity v_k. More energetic ions, accelerated by magnetospheric processes, have much higher impact velocities $v_i \gg v_c$. Eddy current induction from open jovian field lines moving across the satellite ionosphere (largely arising from sputtering of neutrals off the satellite surface) leads to reduced impact speeds, $v_i \sim (v_c - v_k) f_c^{-1}$ with sub-corotation factor $f_c = 5$ for Europa (Sauer *et al.* 1998) and $f_c = 3$ for Ganymede (Williams *et al.* 1998). No estimates of f_c are available for Callisto. For the purpose of numerically tracking motions of incident particles on open field lines near Ganymede in Section 4.3 we use the reduced impact speeds. Within the closed dipole field region of this satellite the sharply reduced plasma density from field line resonance modeling (Volwerk *et al.* 1999) gives a much larger reduction $f_c \sim 50$, such that only a few percent of the corotating plasma particles at low energies may actually impact the equatorial surface. A similar reduction $f_c \sim 60$ was inferred for plasma flow in the downstream wake region of Io (Frank *et al.* 1996).

The incident fluxes of fully or partially corotating particles are expected to be higher on the trailing than the leading sides if there is full access to the surface as demonstrated numerically by Pospieszalska and Johnson (1989). The peak incidence flux can be up to an order of magnitude higher near the trailing apex than elsewhere, and this peak flux is several times larger than the globally averaged flux. Electrons have smaller gyroradii (Section 3.3) and shorter latitudinal bounce periods in the jovian magnetic field than ions at comparable energies, so much of the electron and lower energy ion flux would impact into the trailing hemisphere at higher local intensities than the globally averaged values presented here.

3.3. Gyroradius Effect

Low-energy corotating ions and electrons first impact the trailing hemisphere, but more global irradiation arises in part from the large gyroradii of energetic ions. The maximum gyroradius in km for equatorially trapped (pitch angle $\alpha \sim 90^\circ$) particles is simply calculated from $r_g = P(30B_J)^{-1}$, where P is the magnetic rigidity (particle momentum p divided by charge q) of the particle in megavolt (MV) units and B_J is the local magnetic field magnitude in Gauss (1 G $= 10^5$ nT). Figure 4 gives the kinetic energies E_{gr} at which r_g equals the physical radius r_s of each Galilean satellite for electrons, protons, and the iogenic heavy ions O^{2+} and S^{3+}. In the case of Ganymede the internal dipole moment, $B_G \sim 750$ nT (Section 4.1), gives a larger total, $B \sim 650$ nT, near the satellite equator, so we show values with and without the internal component. Except for those of the low-rigidity electrons, all these energies fall within the range considered here from the Galileo EPD measurements for all the satellites. Significant fractions of the energy flux from heavy ions and higher energy protons would therefore be uniformly distributed onto the satellite surfaces.

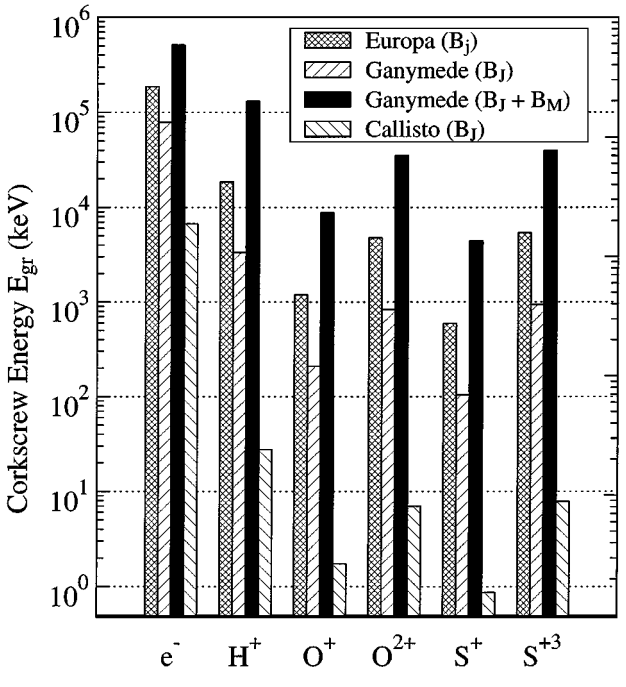

FIG. 4. Corkscrew energies E_{gr} (Section 3.3) at which energetic electron, and selected ion, gyroradii r_g in the ambient jovian magnetic field $\mathbf{B}_J$ equal the satellite radii R_s for Europa, Ganymede, and Callisto. The E_{gr} values for the total external and internal ($\mathbf{B}_J + \mathbf{B}_G$) field of Ganymede are also shown. The ions O^{2+} and S^{3+} are likely dominant components (Section 2.3) of the energetic heavy ion environments near these satellites. For the Ganymede dipole field these energies also correspond to the maximum Størmer cutoff values for incidence at the satellite's equatorial surface from local east as defined in Sections 4.2 and 4.3.

A further consequence of the gyroradius effect is that some incidence trajectories are forbidden due to blocking by other parts of the same surface, particularly for energetic ions moving eastward within a satellite's equatorial region for a jovian magnetic field pointing generally southward in satellite-centered coordinates. For further discussion we define a local horizon system with zenith angle Z_e relative to the local vertical and azimuth angle A_z increasing eastward from local north; these angles give the direction *from which* a particle is incident to a potential impact point. The eastward-moving (from west) direction, defined in the "planetographic" sense of being in the direction of satellite rotation, is then given by $Z_e = 90^\circ$ and $A_z = 270^\circ$ and is also close to the local direction of gyration in the jovian magnetic field. $A_z = 90^\circ$ corresponds to the westward moving (from east) direction. Although ions at the critical energy E_{gr} just circumscribe the satellite surface in the absence of any local magnetic perturbation from the magnetosphere–satellite interaction, impact trajectories in this direction at lower energies will be forbidden. The lower limit E_{gr} on allowed impact energies decreases away from the satellite equator toward zero measure at the poles and also decreases with angular separation from the eastward moving direction for all $Z_e \leq 90^\circ$. This directionality is similar, except for an approximate reversal in azimuth angle phase, to that from the Størmer effect (Section 4.2) for forbidden incidence trajectories in the presence of internal dipole fields.

An increase in gyroradius, particularly for energetic ions, can lead to enhancement of irradiation intensity due to expansion of the radial jovicentric corridor swept by the satellite. A satellite located at jovimagnetic latitude $|\lambda_m| \sim 0^\circ$ sweeps all $\alpha \sim 90^\circ$ particles within a corridor of average half-width $w_s \sim f_g r_s$ with gyroradius enhancement $f_g = (1 + r_g r_s^{-1})$. Here we have roughly allowed for variation with jovian rotation in vertical offset of the satellite center in the corotating frame of the jovian dipole field and for random gyrophase of trapped particles corotating longitudinally past the satellite. When the satellite's vertical offset in this frame is $|\delta z| > r_s$, no absorption of the $\alpha \sim 90^\circ$ particles occurs; this is why we express w_s above in terms of an upper limit. In more general and complex cases a numerical model (e.g., Paonessa and Cheng 1985, Bell and Armstrong 1986, Fillius 1988) is needed to calculate sweeping rates and f_g for anisotropic trapped particle fluxes with time averaging over jovian rotation. New complications now include the internal or induced fields near the satellites. Using EPD spectra very similar to those in Figs. 1 and 2 for Europa and Ganymede, Ip *et al.* (1997, 1998) computed ion sputtering yields from these spectra

(mostly for S and O) with $f_g \sim 2$ based on earlier modeling (Pospieszalska and Johnson 1989). For our simplified ($\alpha \sim 90^\circ$, $|\delta z| > r_s$) example above this f_g value appears plausible for S^{3+} and O^{2+} ions in the EPD response range at the E_{gr} energies in Fig. 4. In what follows we will, however, express calculated parameters proportional to irradiation intensity as lower limits for assumed gyroradius factors $f_g > 1$. The f_g value used by Ip *et al.* (1998) may not be applicable to all irradiation parameters to be discussed here.

4. SURFACE SHIELDING BY MAGNETIC FIELD

4.1. Magnetic Fields of the Satellites

Existence of the internal dipole moment of Ganymede was discovered from magnetometer measurements by the Galileo Orbiter (Kivelson *et al.* 1996, 1997a) and further confirmed by modeling of energetic particle signatures (Williams *et al.* 1997a). The dipole is aligned within $\sim 10^\circ$ of the satellite's south rotational pole and has a variable angle to the local jovian **B** direction. The internal dipole field $B_{eq} \sim 750$ nT $\gg B_J \sim 100$ nT is strong enough to dominate the external field contribution out to about two Ganymede radii, the maximum lateral extent of the Ganymede magnetosphere, and gives rise to closed dipolar field lines within this region as shown in Fig. 5. As discussed below, this configuration significantly affects access of magnetospheric particles to the equatorial surface.

Initial fits of dipole field models to Galileo magnetometer data for Europa and Callisto showed only upper limits, $B_{eq} \sim 120$ and 15 nT, respectively, the actual dipole moments (if any) being poorly determined (Kivelson *et al.* 1997b, Khurana *et al.* 1997). Modeling of later measurements now extending into the Galileo Millenium Mission (GMM) indicate for these latter two satellites the presence of induced dipoles varying for different Galileo flybys in response to change of the external field direction during jovian rotation. A small induced component may be present at Ganymede but is difficult to separate from the internal dipole and the variable magnetospheric field (Khurana *et al.* 1998, Kivelson *et al.* 1999). These induced dipoles are thought to arise from electric currents induced in subsurface water layers, at least for Europa and perhaps Callisto, by variations of the external field, mostly in directions perpendicular to the satellite spin axes. As shown, respectively, in Figs. 6 and 7 for these two satellites, field lines at all points on the surface open out into the magnetosphere, albeit with significant divergences near the induced magnetic poles. Notwithstanding other effects (e.g., corotational impact asymmetry of plasma particles), these open configurations allow free access of magnetospheric particles to all points on the surface of these two satellites.

4.2. Dipole Energy Cutoffs from Størmer Theory

Quantitative relations in analytical form to calculate lower limits on particle energies needed to penetrate a dipole field to any interior point were given originally by Størmer (1955).

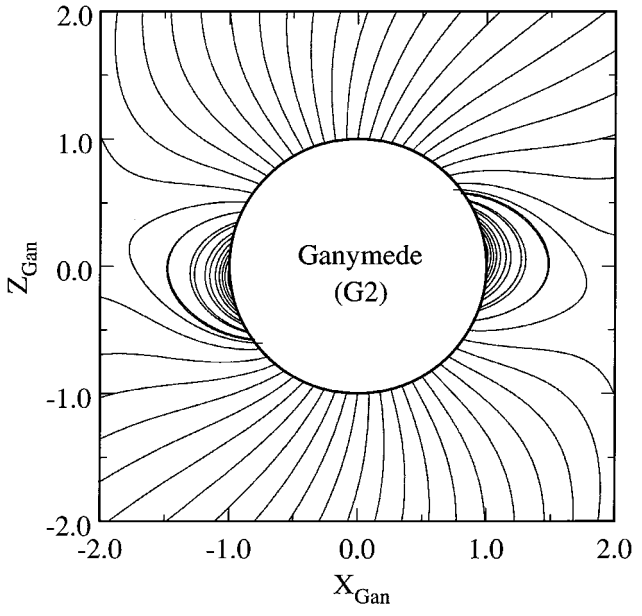

FIG. 5. Magnetic field line configuration around Ganymede from vacuum superposition of the internal dipole field (Kivelson *et al.* 1996, 1997a) and the Khurana (1997) model for the jovian external field at the System III location (Table I) of this satellite during the G2 encounter at closest approach. The field lines are computed in the $\mathbf{X}_s$–$\mathbf{Z}_s$ plane where $+\mathbf{X}_s$ is directed toward Jupiter and $+\mathbf{Z}_s$ is northward. The external field components are strongest in this plane with the $-\mathbf{Z}_s$ component from the jovian dipole field being dominant. The north magnetic pole of Ganymede is tilted 10° away from the satellite's rotational axis toward $\varphi_s = 200^\circ$ in satellite east longitude. The field lines are computed outward from the Ganymede surface at 5° increments in satellite latitude; only the lines with surface footpoints are shown. Field lines closing back to the surface at latitudes $\lambda_s \leq 40^\circ$ define the zone of Størmer deflection (Sections 4.2 and 4.3) for energetic electrons and charged ions from the local magnetospheric environment.

Scaling of these cutoffs for Saturn was given by Cooper and Simpson (1980) and is now applied to Ganymede. The representation below can be applied to any magnetized body with an internal dipole field. In terms of central body radius r_s in kilometers, equatorial surface field magnitude B_{eq} in nT, local horizon directional angles (Z_e , A_z) as defined earlier (Section 3.3), McIlwain (1966) L value, and local magnetic latitude λ_m, the local cutoff P_c in megavolt units of magnetic rigidity (momentum per charge) is given by the relation

$$P_c = 3.0 \times 10^{-4} B_{eq}\, r_s \times [L(1 + (1 + s_q s_d \sin Z_e \sin A_z \cos^3 \lambda_m)^{0.5})]^{-2}. \quad (1)$$

The dipole sign parameter s_d equals $+1$ for approximate alignment of the magnetic dipole and rotational axis vectors in the same directions, as occurs for the planets Jupiter and Saturn, and -1 for approximate alignment in opposite directions as for Ganymede and Earth. Changing the particle charge sign s_q also reverses the directional dependence.

The McIlwain L value in the above relation is exactly the equatorial distance in satellite radii at the local field line's crossing of the magnetic equatorial plane for a pure dipole field. This

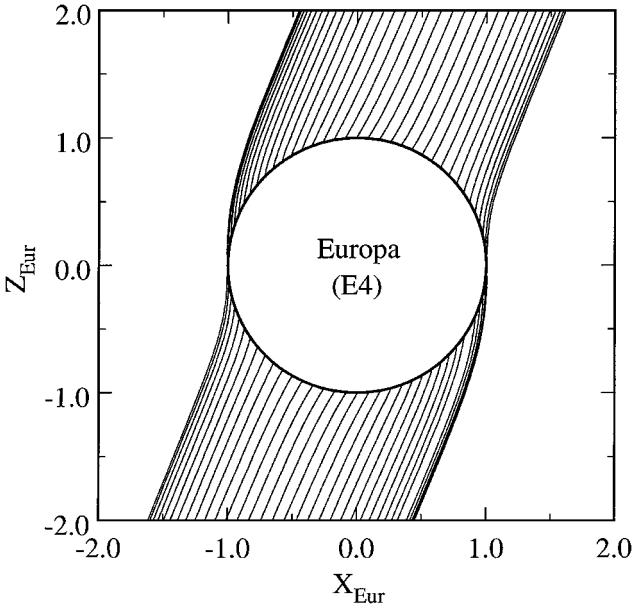

FIG. 6. Magnetic field line configuration around Europa in the $\mathbf{X}_s$–$\mathbf{Z}_s$ plane (cf., Fig. 5) from vacuum superposition of the external jovian magnetic field $\mathbf{B}_J$ (Khurana 1997) at the System III location of the E4 encounter and the induced dipole field as modeled by Khurana *et al.* (1998) and Kivelson *et al.* (1999). Only the field lines with surface footpoints are shown as in Fig. 5; note the absence of any dipolar field lines closing back to the surface. The induced dipole moment $\mathbf{M}_I$ at the satellite equator varies in a direction anti-parallel to the local $\mathbf{X}_s$–$\mathbf{Y}_s$ component of $\mathbf{B}_J$, mainly the $\mathbf{X}_s$ component, and with a magnitude sufficient to give $\mathbf{B}_J + \mathbf{B}_I = 0$ at the induced magnetic poles. The latter are approximately located at the sub-jovian and anti-jovian surface points where inflection points appear in the field lines.

is roughly (Stone 1963) the same distance for a more realistic multipole field in which the dipole provides the strongest component. Sauer and Ray (1963), and later Smart and Shea (1967, 1973), used numerical particle trajectory calculations to generalize the applicability of the L-dependent cutoff to the multipole fields, showing that P_c remains approximately constant along a line of force defined by L at any latitude. We compute finite L and P_c values in the dipole region of Ganymede but assign infinite L values with zero P_c cutoffs to the polar cap region of Ganymede and the entire surfaces of Europa and Callisto.

In the conversion of P_c to total kinetic energy E_c, as given by the relativistic relation

$$E_c = ((P_c\, q)^2 + m^2)^{0.5} - m \qquad (2)$$

for particle charge q, momentum $P_c\, qc$, and mass mc^2 (we use the convention that light speed $c = 1$), the particle charge becomes critically important. Energy cutoffs are shown in Fig. 8 for electrons and various ions species incident from the zenith ($Z_e = 0°$) as computed from Eqs. (1) and (2). The heavy ion cutoffs depend strongly on charge states, here assumed mainly to be O^{2+} and S^{3+} (Section 2.3). In any surface region within the dipole field of Ganymede the magnetospheric electrons are totally excluded for energies measured by the Galileo EPD instrument. Any EPD-energy electrons reaching the surface in the equatorial region would have first become quasi-trapped before precipitating to the surface. Electron trapping near the edge of the dipole region was observed during the G8 Galileo encounter

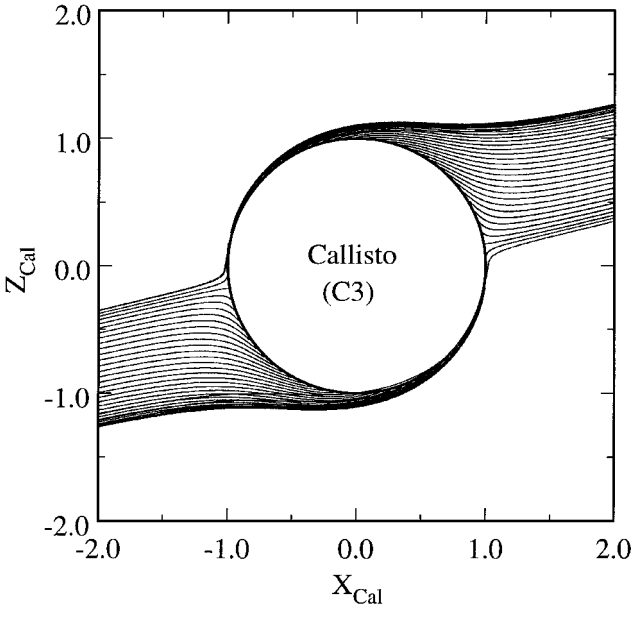

FIG. 7. Magnetic field line configuration (cf. Fig. 6) around Callisto in the $\mathbf{X}_s$–$\mathbf{Z}_s$ plane for superposition $\mathbf{B}_J + \mathbf{B}_I$ of the external and induced fields at the time of the C3 encounter. Only the field lines with surface footpoints are shown as in Figs. 5 and 6. The large relative magnitude of the $\mathbf{X}_s$ component for $\mathbf{B}_J$ induces a strong field line divergence near the satellite. As for Europa (Fig. 6), there is no region of closed field lines.

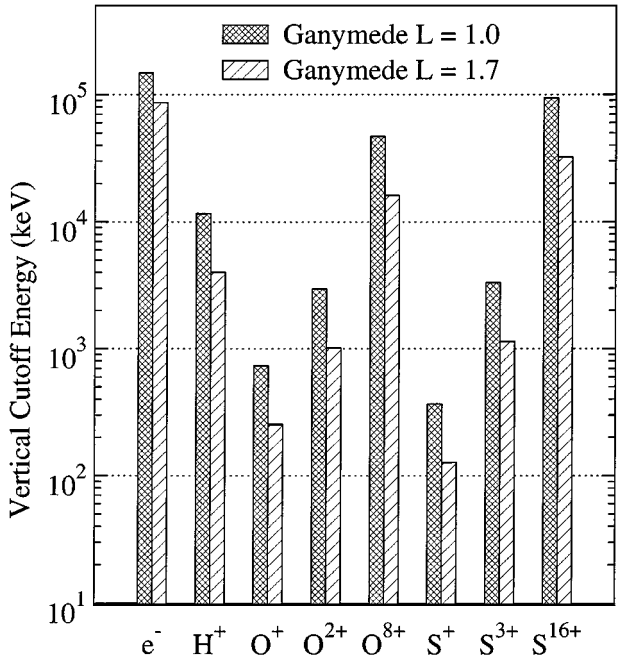

FIG. 8. Størmer cutoff energies (keV) computed from Eqs. (1) and (2) for penetration of electrons and ions to the equatorial ($L = 1.0$) and mid-latitude ($\lambda_m = 40°$ and $L = 1.7$) surface of Ganymede through a pure dipole magnetic field in vacuum with no external jovian field.

and the efficiency for entry of such electrons into the Ganymede magnetosphere appeared to be no more than 1 to 10% (Williams *et al.* 1997b).

The directionality of Størmer cutoffs computed from Eqs. (1) and (2) are now summarized for energetic protons incident onto the equatorial surface of Ganymede for a pure internal dipole model with no jovian field contribution or blockage of incident trajectories by the satellite surface. The cutoffs are maximal for incidence from local east ($A_z = 90^\circ$), minimal from west ($A_z = 270^\circ$), and constant for any direction of incidence within the plane of the local magnetic meridian ($A_z = 0^\circ$ or 180° for any $Z_e \leq 90^\circ$ value). Note again (Section 3.3) that east and west directions are respectively defined in the usual planetographic sense of toward and away from the direction of rotation for the Galilean satellites. A maximum cutoff from East at the equatorial surface corresponds to a particle having a gyroradius equal to the surface radius; that is, a particle of this energy and incidence direction is in a circular magnetic orbit around the satellite.

4.3. Particle Trajectory Results for Ganymede

Numerical techniques are needed to calculate charged particle trajectories in realistic models for the real magnetic environments of the Galilean satellites, for which the simple model of Eq. (1) for a dipole extending to infinity in a vacuum is clearly not valid. These calculations require that the total vector magnetic field, including contributions from all internal, induced, and external sources, be computed at each step along the trajectory. For the external magnetospheric field we use either a simple jovian planetary dipole model (e.g., $B_{eq} \sim 4.3$ G at the equatorial surface of jupiter) or the full magnetospheric model of Khurana (1997). Additional magnetic fields from internal or induced dipoles, and extending outward one radius r_s from the satellite surface, are added to give the total vector **B** field. Distance to the surface must also monitored at each step along a computed trajectory to a desired endpoint to check whether the trajectory is forbidden by surface shadowing.

For this purpose we have implemented our own modifications for the jovian magnetospheric and satellite environments of now-standard trajectory tracing routines, originally implemented by Shea *et al.* (1976) for Størmer cutoff calculations of solar and galactic cosmic ray penetration to the surface of Earth. The principal algorithm involves Runge-Kutta (fourth order) integration *backward* in time of the equation of motion for particles of charge q and vector velocity **v** incident at some endpoint position within the local magnetic field **B** in the corotating frame of the planetary magnetic field $\mathbf{B}_J$. The relative corotation velocity $(v_c - v_k)\ f_c^{-1}$ with sub-corotation factor $f_c \geq 1$ is used to transform the particle position at the end of each step from the corotating frame to satellite-centered coordinates to determine whether an impact has occurred. The default step time is $0.01\tau_g$ with respect to magnetic gyroperiod τ_g computed at the start position of each step but is decreased if the resultant step length becomes too large, e.g., due to large local gradients in any component of **B**.

A particle trajectory tracked back along a direct path, without passing through the satellite surface, to an initial point of origin beyond the assumed magnetospheric boundary is identified as having an allowed trajectory. By varying the particle incidence energy the approximate energy of transition from forbidden trajectories at lower energies to allowed trajectories at higher energies is then defined as the local Størmer cutoff energy E_c for the given endpoint position and direction of incidence. Some trajectories not originating from outside the satellite magnetosphere in a predetermined number of steps (e.g., 10^5) are designated as being associated with locally trapped particles. In the Ganymede environment most trajectories at energies below E_c are identified as forbidden due to surface shadowing, while the relatively few trapped events tend to cluster at energies just below E_c.

The effect of directional cutoffs on incident energy flux is illustrated in Fig. 9 for an incidence point at the equatorial

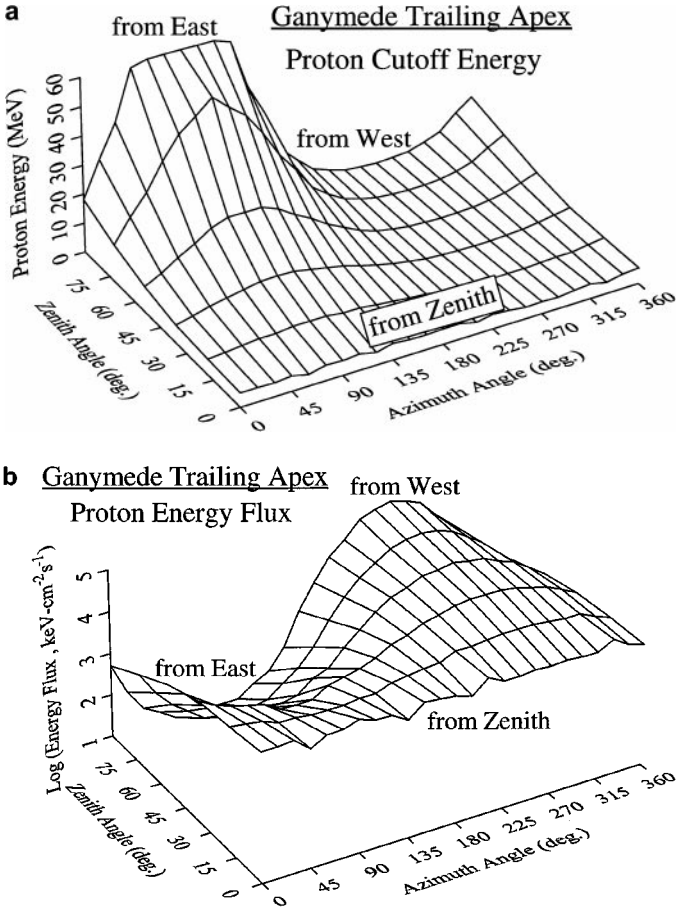

FIG. 9. Directional maps of proton (a) Størmer energy cutoffs and (b) penetrating energy fluxes from numerical calculation for penetration of energetic protons to the trailing apex surface of Ganymede as function of local zenith (Z_e) and azimuth (A_z) angles (Sections 3.3 and 4.2). Energy fluxes are computed from integration of the measured proton spectrum near Ganymede (Fig. 2) in total energy between the Størmer cutoffs and 100 MeV.

surface of Ganymede and at the center of the trailing hemisphere. The 120 incidence directions are chosen for isotropic incidence onto a flat surface from evenly spaced increments of $0 \leq \cos^2 Z_e \leq 1$ and $0 \leq A_z \leq 360^\circ$. Mid-point $(Z_e, A_z)_i$ values are computed for each increment. The particle trajectory code is used to determine all cutoff values E_c $(Z_e, A_z)_i$ in Fig. 9a for protons and energy fluxes in Fig. 9b are calculated from integration over the EPD energy spectrum j_{H+} (E) from Fig. 2. As expected from Eq. (1), the proton energy cutoff is smallest from the westward $(Z_e = 90^\circ,\ A_z = 270^\circ)$ direction where the energy flux is then largest. In the context of surface terrain exposure the east–west asymmetry of the cutoffs means that westward-facing slopes will be more strongly irradiated by penetrating magnetospheric ions than those facing eastward. Electrons would have the opposite directionality but cannot reach the equatorial surface at EPD energies $\gg$10 keV.

The numerical model in principle allows us to map the global dependence of the energy cutoffs in surface latitude–longitude (λ_s, ϕ_s) and incidence direction (Z_e, A_z) coordinates. However, such an undertaking needs to include a more complete magnetic model for the Ganymede environment (e.g., including trailing–leading asymmetries due to compression by the corotating plasma pressure, cross-tail electric fields, etc.). Such calculations are planned but will be computationally intensive. Therefore, a detailed discussion of longitudinal asymmetry is beyond the scope of the present paper.

Figure 10 shows our computed mapping of proton transmission energies to the equatorial Ganymede surface as a function of magnetic east longitude ϕ_m and latitude λ_m for incidence from the local zenith direction at kiloelectron volt to megaelectron volt energies E. Three distinct regions in the plotted E vs ϕ_m and E vs λ_m domains are apparent:

(1) Low energy protons below 20 keV (the EPD response threshold) show the expected longitudinal asymmetry with maximum access to the trailing hemisphere and reduced access to the leading hemisphere. Vertically incident intensities of these corotating particles fall off with increasing λ_m in the closed field region but increase again at the edge of, and outside, this latitudinal region.

(2) No direct transmission occurs near the magnetic equator in the intermediate energy range up to megaelectron volt energies. Proton incidence in this zone comes mainly from trapped particle trajectories originating within the satellite magnetosphere. Narrowing of this forbidden trajectory zone at magnetic latitudes $\lambda_m > 20^\circ$ reflects the λ_M dependence in Eq. (1). Surface incidence from near the vertical direction mostly occurs on open field lines at $\lambda_m > 30^\circ$.

(3) All protons above the Størmer cutoffs at megaelectron volt energies reach the surface with no apparent longitudinal variation, although some leading–trailing asymmetry would likely be induced in more realistic models from magnetic compression by the upstream corotating plasma.

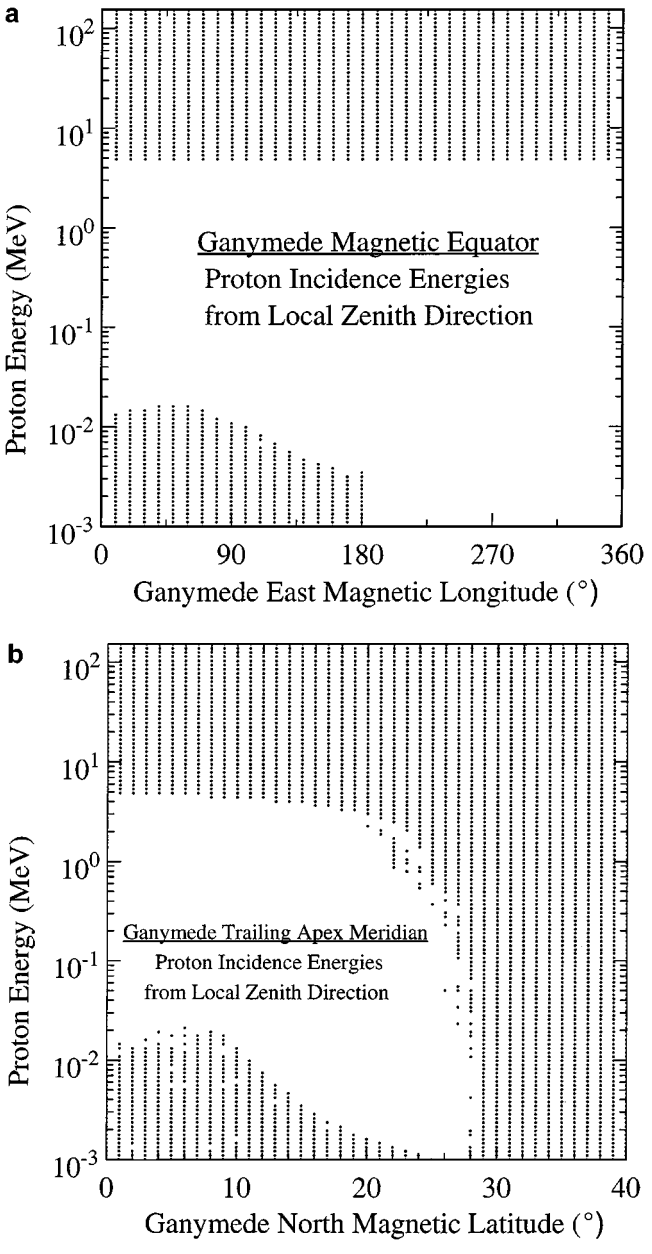

FIG. 10. Magnetic (a) east longitude ϕ_m and (b) north latitude λ_m distributions of proton energies for allowed trajectories incident from local zenith onto the surface of Ganymede. East is defined in the "planetographic" sense (Section 3.3) to be the direction of satellite rotation. The source computation utilizes a dipole approximation for the external Jovian magnetic field $\mathbf{B}_J$ and an internal dipole moment $\mathbf{M}_G$ ($\mathbf{B}_{eq} = 750$ nT) aligned with the southward jovicentric component of $\sim$100 nT of $\mathbf{B}_J$. The longitude and latitude profiles are respectively computed at the satellite magnetic equator and the trailing apex meridian.

5. SURFACE IRRADIATION MODEL

5.1. General

Our calculations for irradiation effects begin with the spin-averaged flux spectra $j_i(E)$ of Figs. 1, 2, and 3 for the EPD

measurements of the ion ($i = 1, 2, 3$ for H^+, O^{2+}, S^{3+}) and electron ($i = 4$) components at the orbits of Europa, Ganymede, and Callisto. In the cases of Europa, Callisto, and the Ganymede polar cap these spectra are directly converted to omnidirectional flux $f(E) \sim \pi j(E)$ in units $(cm^2\text{-}s)^{-1}$ and integrated above the relevant instrument energy thresholds E_0 for any weighting function $w_i(E_0, E)$ applying to a particular irradiation parameter and incident particle type i with no other distinction for incidence location on the satellite surface. For the Ganymede equatorial region the rigidity cutoffs $P(Z_e, A_z)$ from the 120 incidence directions for protons in Fig. 9a are converted via Eq. (2) to equivalent energy cutoffs E_c for heavy ions and electrons, and the energy integral is then summed for each of these directions to give the omnidirectionally averaged parameter value dependent on incidence position (λ_s, ϕ_s). For dosage calculations the vertical depth d in units of grams per square centimeter $(g\text{-}cm^{-2})$ of water ice at unit density is also used; this simplifies discussion of depth-dependent effects even in porous surface ice.

The computed irradiation parameters in Table II include omnidirectional energy integrals at the outer surface of each satellite region for each particle type, and the combined effects of all types if appropriate. Results for depth dependence of volume dosage timescales (cf., Section 5.2) are summarized in Fig. 11. The surface energy integrals give values in Table II for particle number flux, energy flux, sputtering time in years per mm for surface erosion of H_2O molecules, and cumulative implantation time in years to accumulate 10^{16} cm^{-2} stopped ions. The average stopping depths, weighted by flux intensity for each particle type, are also included in Table II. The typical average incident angle corresponding to these depth values is $Z_e \sim 47^\circ$ for averaging over the finite number of incidence directions as compared to the purely isotropic case (Section 3.1). The timescales in years for Fig. 11 refer to times for accumulation of an energy dosage of 100 eV per 16 amu of ice material, a standard cumulative dosage measure (e.g., Strazzulla and Johnson 1991) for laboratory irradiation experiments. If 100 eV is sufficient to chemically modify (Section 9.2) in some way each target molecule, then this cumulative dosage corresponds nearly to complete modification for all ice molecules. In the following sub-sections some details of the irradiation calculation methods are briefly discussed.

TABLE II
Irradiation Parameters at Incidence Surfaces of the Satellite Regions

Satellite region Particle	Stopping depth (mm)	Number flux $(cm^2\text{-}s)^{-1}$	Energy flux (keV cm^{-2} s^{-1})	Ion sputtering time (years mm^{-1})	Implantation time [years-$(10^{16}$ $cm^{-2})^{-1}$]
Europa global					
H^+	1.1×10^{-2}	1.5×10^{7}	1.2×10^{10}	4.4×10^{6}	2.1×10^{1}
O^{n+}	1.8×10^{-3}	1.5×10^{6}	1.8×10^{9}	1.6×10^{5}	2.1×10^{2}
S^{n+}	4.8×10^{-4}	9.0×10^{6}	3.0×10^{9}	1.0×10^{5}	3.6×10^{1}
e^-	6.2×10^{-1}	1.8×10^{8}	6.2×10^{10}	—	2.2×10^{0}
Total	—	—	7.8×10^{10}	6.1×10^{4}	—
Ganymede polar cap					
H^+	2.8×10^{-3}	3.8×10^{6}	1.0×10^{9}	1.6×10^{7}	8.7×10^{1}
O^{n+}	4.6×10^{-4}	1.8×10^{6}	3.2×10^{8}	6.2×10^{5}	1.8×10^{2}
S^{n+}	2.9×10^{-4}	3.2×10^{6}	6.6×10^{8}	4.4×10^{5}	1.0×10^{2}
e^-	1.1×10^{-1}	3.1×10^{7}	3.4×10^{9}	—	1.1×10^{1}
Total	—	—	5.4×10^{9}	2.5×10^{5}	—
Ganymede equator					
H^+	2.6×10^{-1}	5.9×10^{3}	3.2×10^{7}	6.0×10^{11}	5.4×10^{4}
O^{2+}	2.7×10^{-3}	3.7×10^{4}	8.8×10^{7}	3.9×10^{6}	8.7×10^{3}
S^{3+}	2.3×10^{-3}	5.8×10^{4}	1.4×10^{8}	2.0×10^{6}	5.5×10^{3}
e^-	—	—	—	—	—
Total	—	—	2.6×10^{8}	1.3×10^{6}	—
Callisto global					
H^+	1.5×10^{-3}	1.6×10^{5}	2.3×10^{7}	2.8×10^{8}	2.0×10^{3}
O^{n+}	2.6×10^{-4}	2.7×10^{5}	2.6×10^{7}	5.8×10^{6}	1.2×10^{3}
S^{n+}	2.1×10^{-4}	3.6×10^{5}	5.2×10^{7}	5.3×10^{6}	9.0×10^{2}
e^-	4.5×10^{-2}	1.8×10^{6}	1.2×10^{8}	—	1.8×10^{2}
Total	—	—	2.2×10^{8}	2.8×10^{6}	—

Note. Calculated parameters are listed from the irradiation model (Section 6) for ion and electron flux spectra in Figs. 1–3 (Section 2) and for total effects (energy flux, erosion) at the satellite surfaces. Depth units in mm are for unit density ice. All values are for lower limits in the limit of gyroradius sweeping factor $f_g = 1$ (Section 3.2). Note that 1 erg-$(cm^2\text{-}s)^{-1} = 6.24 \times 10^8$ keV $(cm^2\text{-}s)^{-1}$ in terms of energy flux units. Erosion time is from lower limit rate for direct ion sputtering of H_2O molecules. The parameters for the Ganymede equatorial region arise from flux integration above the calculated Størmer energy thresholds (Section 4); other integrals are computed above the EPD thresholds ~20 keV. The JPL model spectra (Divine and Garrett 1983) are used above this threshold for Europa and above 0.7 MeV for Ganymede and Callisto. Upper energy limits of these integrals are 100 MeV for ions and 40 MeV for electrons. For the present model electrons do not reach the Ganymede equator in the integration energy range.

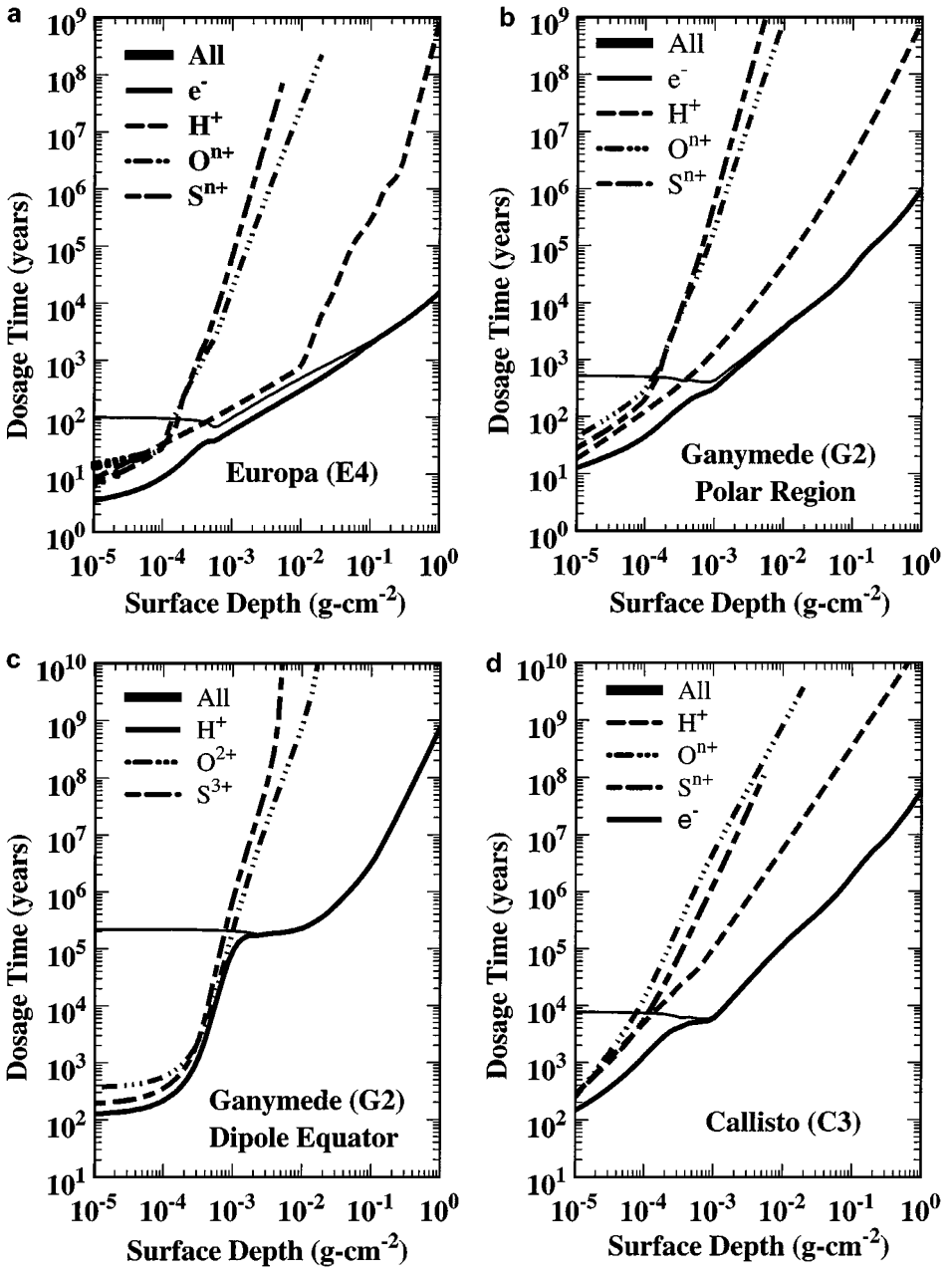

FIG. 11. Time scales in years for accumulation of 100 eV 16 amu^{-1} volume dosages (Section 5.1) as functions of vertical depth at unit water ice density for (a) Europa, (b) Ganymede polar cap, (c) Ganymede magnetic equator, and (d) Callisto. Time vs depth curves are computed for the total dosages and for individual contributions from electrons and from the various ions considered in the present work.

5.2. Energy Loss, Stopping Range, and Volume Dosage

Differential energy loss $\mathrm{d}E(\mathrm{d}x)^{-1}$ rates for ions have been calculated using the SRIM (Stopping and Range of Ions in Matter) code of Ziegler *et al.* (1985) from IBM for ion energies down to ~10 eV. For any desired incident ion type and target material SRIM outputs separate $\mathrm{d}E(\mathrm{d}x)^{-1}$ data for energy loss rates $[\mathrm{d}E(\mathrm{d}x)^{-1}]_{\mathrm{e}}$ due to electronic ionization and $[\mathrm{d}E(\mathrm{d}x)^{-1}]_{\mathrm{n}}$ from nuclear repulsion. The nuclear component is clearly important at eV to keV energies of interest for plasma ion bombardment but the electronic component becomes dominant in the EPD ion energy range. The relative contributions of these two components to total energy loss rate versus incident energy E are shown in Fig. 12. Electron nonradiative $\mathrm{d}E(\mathrm{d}x)^{-1}$ values are computed from differentiation of the electron range vs energy data in Fig. 13. Secondary energy depositions from gamma ray photons produced by radiative (bremsstrahlung) energy losses of megaelectron volt electrons are probably significant at depths

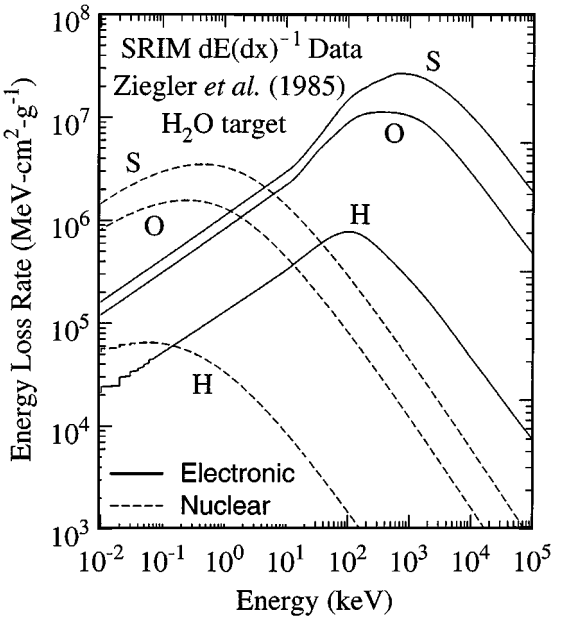

FIG. 12. Electronic and nuclear components of differential energy loss rates $dE(dx)^{-1}$ in units MeV cm^2 g^{-1} for H, O, and S ions passing through H_2O liquid from output of SRIM code (Ziegler *et al.* 1985). We assume negligible differences in these units for the solid phase of H_2O.

$d \gg 1$ cm but the present work covers energy losses only at $d \leq 1$ cm and electrons from the measured (EPD) spectra used here mostly stop within that range.

After selection in sequence of each of 120 incidence angles $\beta_i = Z_e$ for directional integration, the algorithm continues for computing deposited energy versus depth from each particle type. The incident particle spectrum is divided into $N_e \sim 300$–400 logarithmic energy intervals ΔE_j. The target depth range of $10^{-5} \leq d \leq 10^2$ in mass column density (g cm^{-2}) units is similarly divided into 100 logarithmic intervals Δd_K. This division gives equal weight to each decade of incident energy and depth. Each test particle is then given a differential weight $\varpi(E_j) = \pi j(E_j)\Delta E_j N_d^{-1}$ for $N_d = 120$ incidence directions.

Projected ranges, $R_p(E_j)$, for ions from Ziegler *et al.* (1985), and for electrons, are used to determine the stopping depths d_K for initial energy E_j and incidence at angle β_i into the model surface layer, composed of 100% water ice at unit density. In each preceding depth interval Δd_K for integer $k \leq K$ the energy deposition rate is computed from $\varpi(E_j)$ and the electronic energy loss $\delta E_k \leq \Delta E_k$ in that depth interval. The small nuclear energy loss at EPD energies is subtracted to give the electronic δE_k for ions and is of course ignored for electrons. In units of 100 eV 16 amu^{-1} per year the total omnidirectional dosage rate at any depth d is computed from summing over all electronic energy losses from each of the $N = N_e N_d$ test particles. These dose rates are then inverted to give dose timescales for the curves in Fig. 11.

The implantation rates for stopping particles are calculated from summations of differential values for stopping column density $\varpi(E_j)\Delta d_k$ in each depth interval. The cumulative column density I_K in units cm^{-2} year^{-1} to any depth d_K is then found from final summation over all preceding depth intervals $d_k \leq d_K$. In the present paper we only use the maximum cumulative column densities for potential comparison to observational limits in column density units. For each particle type the times in years required to produce cumulative implantation densities of 10^{16} cm^{-2} are given in Table II. For only S^{3+} the depth profiles of cumulative column density in each satellite region are shown in Fig. 14 and indicate that direct sulfur implantation is only significant to micrometer depths.

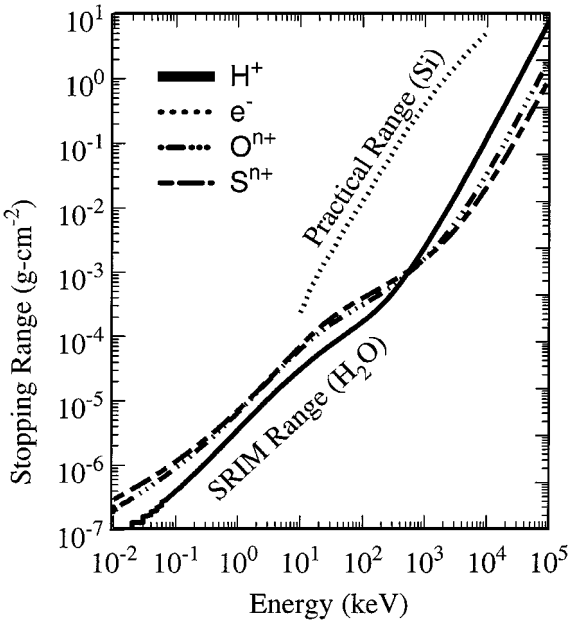

FIG. 13. Stopping ranges (g cm^{-2}) versus energy (keV) in H_2O liquid (or ice) of H, O, and S ions from output of SRIM code (Ziegler *et al.* 1985). Practical ranges for electrons are from laboratory data for measured ranges in silicon.

5.3. Sputtering

Surface erosion by sputtering has been extensively reviewed by Johnson (1990, 1995, 1998) and is dominated at EPD particle energies ≥20 keV by the heavy ions, particularly sulfur. For high $dE(dx)^{-1}$ produced by such ions up to megaelectron volt energies the sputtering process is relatively explosive, removing thousands of water molecules per incident ion. Sputtering yields per incident ion for H_2O for "H-like" and "O-like" ions were compiled by Shi *et al.* (1995) from laboratory measurements and are used here for H^+ and O^{2+}. These same yields were used in the earlier work of Ip *et al.* (1997, 1998) for sputtering on Ganymede and Europa.

Previous work to date has assumed that S sputtering is O-like, due to the difficulty of working with corrosive sulfur compounds in high vacuum experiments. Using an extrapolation procedure, we have derived an approximate yield function for sulfur ions from data for O^+ and Ar^+ ion sputtering. The yields for H^+ and O^+ from Shi *et al.* (1995) have also been extrapolated, above

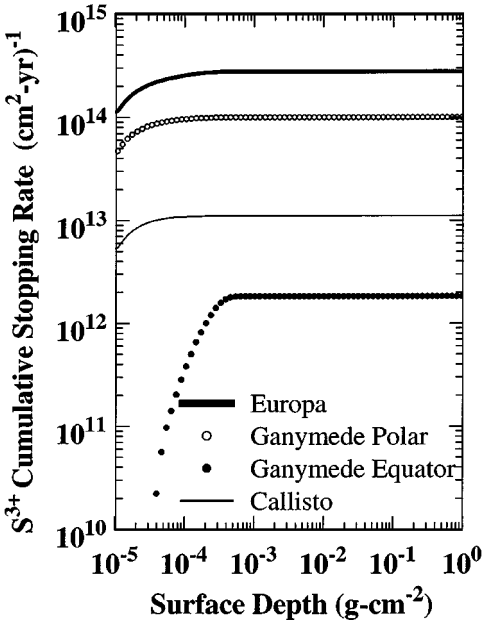

FIG. 14. Total column density above the depth shown of implanted S^{n+} (S^{3+} for Ganymede) accumulated per year for the surfaces of Europa, Ganymede's pole and equator, and Callisto.

1 MeV for H^+ and 16 MeV for O^+, to higher energies $\leq$100 MeV in the limit that $Y_e \propto [dE(dx)^{-1}]^2$ at these energies. There is a weak dependence on charge state which we ignore. [We note one correction to Table 2 of Shi *et al.* (1995): the column labeled "Total Sputtering Rate" is in fact multiplied by 0.25 to allow for porosity as stated in the footnote.]

6. SURFACE ENERGY FLUX

6.1. Irradiation Input

Whereas the heavy ions dominate sputtering, energy deposition leading to chemical alterations at depth is dominated by the light particles. In all cases, except Ganymede's equator, the energetic electrons dominate the total surface energy flux but bombard mainly the trailing hemisphere. Protons are of secondary importance at the Ganymede polar cap but the heavy ions dominate the protons on Callisto.

At the Ganymede dipole equator the EPD electrons cannot penetrate from the jovian magnetosphere and the energetic proton component is only 12% of the total $\sim 3 \times 10^8$ keV (cm^2-s)$^{-1}$, giving a pole to equator ratio of an order of magnitude and a highly dominant irradiation by the heavy ions in the equatorial region. Frank *et al.* (1997) quoted an energy flux $\sim 6 \times 10^8$ keV (cm^2-s)$^{-1}$ for warm plasma (70 eV–4.5 keV) electrons over the Ganymede polar cap. If this component also impacts the equatorial region, the total polar and equatorial energy fluxes then become 5×10^9 and 9×10^8 keV (cm^2-s)$^{-1}$, respectively. This polar-equatorial ratio $\sim$5 is close to the value $\sim$4 already cited by Delitsky and Lane (1998) from our preliminary work for this paper (Cooper *et al.* 1997a,b). However, the actual ratio may be closer to that for the energetic particles alone, due to apparent depletion of plasma particles within the Ganymede magnetosphere from the Volwerk *et al.* (1999) work. The Ganymede surface may therefore be relatively protected from plasma bombardment but much more exposed to the energetic kiloelectron volt and megaelectron volt particles at energies respectively below and above the Størmer "forbidden" zone in Fig. 10.

6.2. Solar Insolation

The comparative energy fluxes from solar irradiation are given in Table III as compiled from solar UV irradiance tables for 1 AU in Hall *et al.* (1985), converted to keV (cm^2-s)$^{-1}$ units, and reduced for globally averaged insolation of the jovian satellites at 5.2 AU from the Sun. The total solar irradiance varies by 0.1% over 11-year solar cycles with 10–20% of this variation occurring in the UV (Lean 1997, Lean *et al.* 1997). For the present discussion we ignore UV variability over all time scales for satellite irradiation. The total solar insolation of $S_J \sim 8 \times 10^{12}$ keV (cm^2-s)$^{-1}$ is of interest mainly for modeling of surface temperature. For Europa a visible albedo $A \sim 0.6$ for energy flux $\sim 3 \times 10^{12}$ keV (cm^2-s)$^{-1}$ at wavelengths $\lambda \sim$ 4000–7000 Å gives $(1 - A)S_J \sim 2 \times 10^{12}$ keV (cm^2-s)$^{-1}$ for the absorbed energy flux, mostly reemitted in the infrared, while at Callisto for $A \sim 0.2$ the absorption is twice that for Europa.

TABLE III
Globally Averaged Surface Irradiation of the Galilean Satellites

Irradiance band, radiolysis process, or surface region	Wavelength range (Å)	Energy range (eV)	Energy flux (keV cm^{-2} s^{-1})
Red to IR	>7000	<1.8	3.7×10^{12}
Visible (PAR)	4000–7000	3.1–1.8	3.4×10^{12}
UV-A	3200–4000	3.9–3.1	6.7×10^{11}
UV-B	2800–3200	4.4–3.9	9.5×10^{10}
Europa	—	—	$\mathbf{7.8 \times 10^{10}}$
UV-C	1000–2800	12.4–4.4	4.0×10^{10}
Ganymede polar	—	—	$\mathbf{5.4 \times 10^{9}}$
H_2O (ice) dissociation	<2067	>6	7.6×10^{8}
Ganymede equator	—	—	$\mathbf{2.6 \times 10^{8}}$
Callisto	—	—	$\mathbf{2.2 \times 10^{8}}$
O_2 production by e^-	<1250	>10	3.8×10^{7}
EUV	<1000	>12.4	1.2×10^{7}
O_2 (gas) dissociation	<410	>30	7.9×10^{6}

Note. Energy fluxes I_1 integrated within selected wavelength bands of the solar irradiance spectrum $S_1(\lambda)$ at 1 AU (Hall *et al.* 1985) are rescaled to $I_5 = I_1(5.2)^{-2}$ for the jovian system to give globally averaged insolation $I_s = 0.25 I_5$. For reference the total irradiance at 1 AU in more commonly used units is 1.37 kW m^{-2} or 1.37×10^6 erg (cm^2-s)$^{-1}$ as compared to 8.55×10^{14} keV (cm^2-s)$^{-1}$ in the units used here for comparison to particle energy fluxes. The PAR (photosynthetically active radiation) range is of potential interest as an energy source for Earth-like life forms while UV-B might be harmful. The H_2O dissociation and O_2 production thresholds are respectively from the Orlando and Kimmel (1997) and Sieger *et al.* (1998) measurements for electron irradiation of water ice. The total energy fluxes of energetic particles from Table II for each satellite surface region are shown in bold for comparison.

Since the irradiation levels for the equatorial and polar cap regions of Ganymede are likely very different, the solar UV energy flux must be separately computed for meaningful comparisons in these two regions. The longitudinally averaged extent in latitude of the equatorial band is $|\lambda| \leq 40^\circ$, the zone of closed dipolar field lines, for exclusion of electrons and $|\lambda| \leq 30^\circ$ for ions. Using the electron boundary, we then calculate analytically that the ratios of regional to global insolation, averaged for diurnal rotation relative to the Sun, are ~0.8 for the polar cap and ~1.2 for the equatorial band. The polar cap value is of course mostly weighted toward insolation at mid-latitudes.

Energies $E_v > \sim 4.4$ eV (wavelengths $\lambda_v < 2800$ Å) are required to dissociate H_2O, OH, and H_2O_2 (Johnson and Quickenden 1997, Carlson *et al.* 1999b, Delitsky and Lane 1998). Laboratory experiments indicate thresholds in water ice ~6 eV (Orlando and Kimmel 1997). The Europa particle flux (Table II) exceeds that from solar UV irradiation at $E_v > 4.2$ eV. The equivalent photon energies for the Ganymede polar and equatorial regions are 5.4 and 6.5 eV, respectively, the latter also applying to Callisto. Whether or not the particle energy flux is dominant will depend on the particular chemical reaction in question. The decline in UV insolation toward the satellite poles (see above) and magnetic deflection of low-rigidity particles away from the Ganymede equator provide further relative enhancements of particle irradiation effects over those from UV in the polar surface regions.

6.3. Subsurface Heat Flow

Present radiogenic heat flows at the satellite surfaces in standard units of erg $(cm^2\text{-s})^{-1}$ [6.2×10^8 keV $(cm^2\text{-s})^{-1}$] are 7.2 (Cassen *et al.* 1979), 4.8 (Cassen *et al.* 1980), and 3.8 (Cassen *et al.* 1980) for Europa, Ganymede, and Callisto, respectively. Note that these exceed energy fluxes from magnetospheric irradiation (Table II) only for Ganymede's equator and for Callisto. Passey and Shoemaker (1982) required a radiogenic heat flux ~10 erg $(cm^2\text{-s})^{-1}$ at Ganymede's surface to reduce lithospheric viscosity for topographic relaxation of crater walls at a time $\sim 3.7 \times 10^9$ years ago near the estimated time of formation for grooved terrain. Primordial heat flows from the radiogenic source were about eight times higher than now (Cassen *et al.* 1980), but would have been comparable to, or greater than, irradiation energy fluxes at present levels only for Ganymede and Callisto.

Tidal heat flows needed in the outer ice crust of Europa to keep the underlying ocean from freezing are 20 to 60 erg $(cm^2\text{-s})^{-1}$, dependent on models (e.g., Squyres *et al.* 1983, McKinnon 1999, Showman and Malhotra 1999), while heat from this source is negligible at Callisto. About 15 erg $(cm^2\text{-s})^{-1}$ would have been required to melt Ganymede's mantle ice but radiogenic heating would have supplied this only in the first 5×10^8 years (Cassen *et al.* 1980, Showman *et al.* 1997). Transient tidal heating up to $\sim 10^2$ erg $(cm^2\text{-s})^{-1}$ from eccentricity-pumping resonance might have produced episodic resurfacing on Ganymede at later times (Showman and Malhotra 1997, Showman *et al.* 1997). Interestingly, the total of the present radiogenic (above) and irradiation (Table II) energy fluxes for Ganymede's polar cap is close to that needed for a modern Ganymede ocean.

6.4. Meteoroid Impact

Energy input from meteoroids can, in comparison, be estimated from approximations used for impacts on Saturn's rings by Cuzzi and Estrada (1998) with more general applicability to Jupiter as well as Saturn. Using compilations of meteoroid mass distributions from various sources, these authors determined an interplanetary mass flux $d\sigma(dt)^{-1} \sim 5 \times 10^{-17}$ g $(cm^2\text{-s})^{-1}$. Burns *et al.* (1999) recently used this same mass flux to account for origin of the jovian rings by meteoritic erosion of dust from small satellites near the rings. Much of the interplanetary mass flux is in particles of size 10–100 μm. For a typical interplanetary velocity $v_\infty \sim 14$ km s^{-1}, and a jovian escape velocity $v_{esc} \sim 19$ km s^{-1} near the orbit of Europa, the Öpik (1951) gravitational focusing factor is $f_G = 1 + (v_{esc} v_\infty^{-1})^2 \leq 2.8$ at the orbits of Europa, Ganymede, and Callisto. With an average impact velocity $v \sim v_{esc}$ into the satellite surfaces the maximum energy is then $0.5\, v^2 f_G\, d\sigma(dt)^{-1} \sim 1.5 \times 10^5$ keV $(cm^2\text{-s})^{-1}$, several orders of magnitude less than even the EPD particle energy fluxes for Ganymede's equator and Callisto. Further allowing for order-of-magnitude uncertainties in the meteoroid fluxes will likely not change this basic result. Meteoroid energy effects might appear locally around individual large craters but are not significant for the global energy influx onto any of the Galilean satellites. Passey and Shoemaker (1982) found that this heat source was far smaller at 0.07 ergs $(cm^2\text{-s})^{-1}$ [4×10^7 keV $(cm^2\text{-s})^{-1}$] than radiogenic heating (Section 6.3) even during late heavy bombardment at 3.9×10^9 years ago.

6.5. Energetic Neutral Atoms

Charge exchange reactions of plasma ions in the Io torus lead to emission of iogenic neutrals (S, O, Na) into the outer magnetosphere and interplanetary space. Time variability of UV absorption from sulfur on the leading Jupiter-facing quadrants of Europa (Domingue and Lane 1998) and Callisto (Lane and Domingue 1997) has been suggestive of bombardment by the neutral sulfur. Eviatar and Barbosa (1984) estimated that 5×10^{28} low-energy neutrals would be emitted per second with an energy loss rate from the torus of 5×10^{12} W.

The loss rate for ENAs at energies >14 keV was estimated at 1×10^{25} s^{-1} by Eviatar and Barbosa (1984). Using the torus energy loss rate for the thermal S neutrals, we compute maximum S energy fluxes for S to O ratio ≤0.4 (Hall *et al.* 1994) of 2×10^5, 9×10^4, and 3×10^4 keV $(cm^2\text{-s})^{-1}$ at the orbits of Europa, Ganymede, and Callisto with the assumption that the torus neutral emissions are isotropic. The neutrals would bombard only the Jupiter-facing hemisphere of each satellite, and the globally averaged surface fluxes would be ~0.3 of these values. The energy inputs from iogenic neutral atoms are therefore comparable to those from meteoroids and are also far below those from charged particle irradiation in all cases.

7. IMPLANTATION OF SULFUR IONS AND ENERGETIC NEUTRALS

7.1. Observational Evidence

The iogenic heavy ions can provide a source for sulfur observed as SO_2 on the outer surfaces of the icy Galilean satellites. The evidence for this has been the observation of SO_2 in the surfaces of the satellites (Lane *et al.* 1981, Nelson *et al.* 1987, Noll *et al.* 1997a). Galileo NIMS observations in the near infrared (McCord *et al.* 1997, 1998b) show an SO_2 component of nonice features more confined to visibly dark regions on Callisto, Ganymede, and possibly Europa. On the latter the dark regions are the likely locations of emergence for endogenic sources of hydrated mineral, tentatively identified as salts containing sulfur, carbon, and magnesium (McCord *et al.* 1998a, 1999). The correlation of SO_2 with the dark terrain was recently explained by a radiation-induced sulfur cycle involving either endogenic or exogenic S (Carlson *et al.* 1999a).

Europa. Resurfacing of Europa from an internal ocean source of water was originally invoked by Squyres *et al.* (1983) to account for the equilibrium SO_2 column density $\sim 10^{16}$ $(cm^2\text{-}s)^{-1}$ at surface depths of 40–5000 Å accessible to solar UV observations via the International Ultraviolet Explorer (IUE) mission (Lane *et al.* 1981). IUE observations of Europa were extended with long-term studies of time variability (Domingue and Lane 1998). Galileo UVS observations of Europa at maximum spatial resolution (Hendrix 1998) indicate correlations to dark mottled terrain and linea located away from the apex of the trailing hemisphere. Low-resolution UVS observations do show the general peak in absorption near the trailing apex (Hendrix 1998) as predicted by the numerical model of Pospieszalska and Johnson (1989). The temporal UV brightening reported by Domingue and Lane (1998) occurs not in the trailing hemisphere, as expected from magnetospheric variations, but in the Jupiter-facing quadrant of the leading side. This is potentially suggestive of variability in bombardment there by ENAs (Section 6.5). Another possibility is that distortion of the Jovian magnetic field near Europa, due to ionospheric coupling and Alfven wing formation (Paranicas *et al.* 1998), might produce a significant curvature drift of S ions into this quadrant.

Ganymede and Callisto. Ultraviolet SO_2 absorption has also been identified on Ganymede (Domingue *et al.* 1998) and Callisto (Lane and Domingue 1997, Noll *et al.* 1997a). The Ganymede absorption was detected by IUE only in the 1984–1986 epoch of observations discontinuously spanning 1979 to 1996. The 1984–1986 feature had an incomplete correlation to longitudes in the trailing hemisphere, being more visible in the anti-jovian quadrant, which appears to rule out the neutral S source. The IUE feature was absent in 1996 when Noll *et al.* (1996) reported O_3 in the trailing hemisphere; this might argue against a magnetospheric origin for the SO_2 on Ganymede (Domingue *et al.* 1998). However, detailed modeling (Cooper and Bell 1999) of kiloelectron volt ion trajectories impacting Ganymede's trailing hemisphere does support the magnetospheric explanation; reduction of corotation speed near the satellite (Section 3.2) preferentially inhibits access of such ions to the anti-jovian quadrant. The Callisto features appear on the leading hemisphere and with maximum IUE absorption seen on the Jupiter-facing side near the Valhalla impact region Callisto (Lane and Domingue 1997), the latter being suggestive of a neutral bombardment component as at Europa.

7.2. Magnetospheric Ion Implantation

The calculated magnetospheric inputs of implanted S^{n+} ions and other species from the EPD spectra are given in Table II. H and O ion implantation might be relevant to radiation chemistry in refractory material in older dark regions on Ganymede and Callisto, where most of the water ice has sublimed or been sputtered away. The calculated implantation times for cumulative column density 10^{16} ion cm^{-2} range from ~40 years on Europa and on Ganymede's pole to ~6000 years at the latter's equator, not including other amplifying factors such as gyroradius (Section 3.3). Addition of implantation fluxes from corotating thermal ions would decrease these times. Ip *et al.* (1998) quoted a time of seven years for implantation of sulfur plasma ions at the same column density on Europa. Changes in plasma implantation rates, perhaps related to changes in local corotation speed, might account for the UV time variations in the absence of internal source activity.

7.3. ENA Implantation

Implantation of iogenic sulfur neutrals would be unaffected by the planetary and Ganymede magnetic fields; this could be important on Ganymede's Jupiter-facing leading quadrant. Viewed in jovicentric coordinates corotating with Jupiter, the emitted neutrals from the torus follow a spiral (garden sprinkler) trajectory bending in the retrograde direction and impacting preferentially in this quadrant. The 5×10^{28} torus emission rate of Eviatar and Barbosa (1984) gives $\sim 4 \times 10^5$ cm^2 s^{-1} neutrals at the orbit of this satellite and requires only 900 years, as compared to 5500 years for EPD S^{n+} from Table II, to implant 10^{16} cm^{-2} neutrals at the sub-jovian point on the surface. The globally averaged rate for neutral implantation near the equator would be closer to that from the local magnetospheric ions. Corresponding times for 10^{16} cm^{-2} neutral implantation at the sub-jovian points of Europa and Callisto would be about 400 and 2800 years, respectively, much slower than ion implantation.

8. VOLUME DOSAGE AND SURFACE INSTABILITY

8.1. Energy Deposition vs Depth

The depth profiles in Fig. 11 for chemical processing at the level ~100 eV 16 amu^{-1} indicate different layers and timescales of volume dose effects for the energetic heavy ions, protons, and electrons. The most rapid chemical changes occur within the sub-micrometer layer affected by the short-range oxygen

and sulfur ions. These ions can cause total dissociation of target molecules and dominate the sputtering rates in Table II. The electrons, H^+ ions, and UV photons do not sputter or cause damage as efficiently. However, these lightly ionizing components of irradiation may do most of the observed damage. The UV energy flux (Table III) affects only the sub-micrometer layer, mean penetration depth for Ly-α UV photons ($\lambda = 1216$ Å, $E_v = 10.2$ eV) being 0.04 μm (Warren 1984). Table II indicates that the energy flux of energetic charged particles is mostly carried by the protons and electrons, except near the Ganymede equator, and more so by the electrons, particularly if the spectra are extended to MeV. At depths of several micrometers, the proton energy deposition becomes dominant but is overwhelmed by the highly penetrating electrons at all greater depths.

Inclusion of gamma ray production by $\geq$10 MeV electrons would allow extension of the energy deposition profiles to meter depths. Electron dosage times at $\sim$1 m for Europa (R. Evans, unpublished data, Jet Propulsion Lab., 1999) would be equivalent to the $\sim 10^9$-year value in Fig. 11a for 100 MeV protons reaching centimeter depths. Energy deposition at meter depths would also arise from secondary neutrons produced by nuclear interactions of >100 MeV magnetospheric and cosmic ray protons in the water ice (Cooper 1983, Cooper *et al.* 1985). The relatively low energy fluxes of deeply penetrating particles make these sources insignificant for the present work at optical depths but become important at regolith depths $\leq 10^1$ m (Section 8.3).

At even greater depths the slow decay of radioisotopes at low concentrations in interior ice must also be considered. Calculations of Draganić *et al.* (1984) indicate dose accumulations of 1.4×10^3 Megarad (see legend to Fig. 16) or 0.023 100 eV 16 amu^{-1} over 4×10^9 years from such decays in mixed ices deep within comets. The total deposition rate $\sim 6.9 \times 10^8$ keV (cm^2-s)$^{-1}$ from this source in a 10-km ice crust is only about 1% of that from magnetospheric irradiation (Table II) of the millimeter-thick optical layer Europa, and 13% at Ganymede's polar cap, but is about three times the magnetospheric input at Ganymede's equator and on Callisto.

8.2. Surface Erosion by Ion Sputtering

Icy satellites undergo direct magnetospheric and UV irradiation, meteoroid and ENA bombardment, and thermal sublimation, all contributing to surface erosion. The erosion rates depend on the efficacy of these various processes and the availability of fresh ice to replace that lost to space. Direct dissociation of ice and nonice molecules by irradiation to form more volatile constituents promotes chemical erosion, while large $dE(dx)^{-1}$ energy loss rates (Fig. 12) of magnetospheric ions and ENAs produce local erosion by direct sputtering as addressed in Section 5.3. While $\sim$20–30% of the H_2O molecules locally removed by sputtering may escape permanently from the satellite (Johnson 1990, Table 4.4), the bulk of the locally eroded material is returned and redistributed across the surface. Ion sputtering produces long ballistic trajectories of ejected molecules extending over hundreds of kilometers (Sieveka and Johnson 1982, Johnson *et al.* 1983).

Sputtering competes with thermal transport and micrometeorite erosion and transport. Shoemaker *et al.* (1982) found no clear topographic evidence on Ganymede for substantial erosion of surface features by sputtering and suggested that early upper limits on sputtering rates from Pioneer energetic particle data (Lanzerotti *et al.* 1978) were too high. Moore *et al.* (1999) also found no direct evidence for substantial mass movement there due to sputtering.

Thermal effects result in migration of material from warm, dark ice to cold, bright ice (Spencer 1987a) and from warmer sunlit equatorial regions towards colder mid-latitude regions (Purves and Pilcher 1980, Johnson 1985). Meteoritic impacts also displace water molecules forming micro-craters with extended ejecta blankets extending out a couple of crater diameters (Spencer 1987a). For Callisto the minimal coverage by bright water ice and the high abundance of ancient craters indicates dominance by thermal segregation and impacts. Ganymede's surface appears differentiated between a darker equatorial region, where thermal effects likely dominate, and brighter polar regions more intensely irradiated by magnetospheric particles (Johnson 1985, 1997). The more uniformly bright surface at all latitudes on Europa could suggest that sputtering inhibits segregation (Spencer 1987a). The primary modes of crater erosion in times of $\sim 10^7$ years on Europa appear, however, to be surface disruption by diapiric convection, tidal stress fracturing, and some instances of upwelling of subsurface low-viscosity material, possibly liquid water.

Sputtering may either concentrate or further dilute molecular products of volume dosage and implantation, depending on how well the molecules are mixed into water ice and the other surface materials (Johnson 1990, pp. 150–152). One way of directly sampling the molecular composition of the ice without setting a lander down on the surface might be to measure composition (Johnson *et al.* 1998) of the sputtered molecules from the planned Europa Orbiter. If such mixing does not occur, however, the less volatile material becomes preferentially concentrated as in the dark irradiation mantles of comets (Johnson *et al.* 1987) or in the dark, possibly carbonaceous (Carlson 1999), regolith of Callisto.

Thermal mapping at the Europan equator by Spencer *et al.* (1999) indicated a diurnal and seasonal average at low latitudes of 106 K over a range of 82 to 132 K. Generally lower temperatures <100 K were found on the nightside hemisphere and at high latitudes. By Eqs. (4) and (5) in Spencer (1987a) the sublimation time at 106 K for a 1-mm optical layer is $\sim 1 \times 10^7$ years, which we take approximately as the global average. At the peak temperature of 132 K in darker dayside regions, however, sublimation time is only about 400 years. Disk-averaged temperatures of sublimating H_2O ices from Earth-based observations are $\sim$124 K on Ganymede and $\sim$115 K on Callisto (Grundy *et al.* 1999), respectively corresponding to sublimation times of 6×10^3 and 2×10^5 years but associated with relatively smaller fractional

coverages of ~50% and 10–20% of H_2O ice as compared to more homogeneous coverage by H_2O ice mixed with nonice contaminants on Europa (Spencer 1987b). Times to sublimate an H_2O mass equivalent to a globally uniform millimeter layer on the two outer satellites would be 1×10^4 and $1–2 \times 10^6$ years, respectively.

In comparison, Table II gives 6×10^4 years mm^{-1} from the EPD ion spectra for icy regions of Europa, 3×10^5 (1×10^6) years mm^{-1} for pure H_2O ice in the Ganymede polar (equatorial) region, and 3×10^6 years mm^{-1} only for patches of such ice on Callisto. The Europa sputtering time is probably an upper limit, since we include only sputtering of H_2O molecules and use a unit value for the gyroradius factor f_g (Section 3.3). Ip *et al.* (1998) used similar EPD ion spectra to those in Fig. 1 but computed a local sputtering rate for Europa corresponding to 1×10^3 years mm^{-1} (or 1 year μm^{-1}) as an upper limit after adjusting for $f_g \sim 2$, additional sputtering of O_2, and secondary sputtering ($\times 10$) by O_2^+ pickup ions in the europan ionosphere. Sauer *et al.* (1998) indicated that the latter is likely a small effect due to reduced corotational flow near the satellite. Also, the O_2 to H_2O sputtering ratio ~0.6 as used by Ip *et al.* (1998), who cite laboratory data of Bar-Nun *et al.* (1985) for sputtering by 1-keV ions, is too high by a factor of four (Brown *et al.* 1982) for energetic ions up to megaelectron volt energies. For the Ganymede polar region we are in agreement on the sputtering rate with Ip *et al.* (1997), while additional sputtering of O_2 from the bright polar ice would increase the rate slightly.

Taking into account the different fractional coverage by H_2O ice, we confirm from the new particle data the earlier conclusion of Spencer (1987a) based on Voyager measurements. Sputtering is predicted to dominate sublimation and thermal segregation effects only on Europa. This could account for the general brightness of that satellite through global redeposition of sputtered H_2O as high-albedo frost. Therefore, the brightening with age of dark regions on Europa may be due to direct radiation damage and frost overcoating or to H_2O molecular reabsorption into irradiated mineral hydrates common to these regions (Section 9.3).

8.3. Meteoritic Gardening

The recent Galileo Orbiter discovery (Krüger *et al.* 1999) of a dust ring around Ganymede and observed presence of dust around Europa and Callisto argue for continuing regolith growth from micrometeoroid effects by impact gardening of the surface (Shoemaker and Wolfe 1982). Due to preferential bombardment of the leading hemispheres, regolith depths there for Ganymede extend to ~20 m at the apex and down to ~1 m on the trailing side (Shoemaker *et al.* 1982). The global average depth is about ~10 m. The latter authors note that the ejecta rays are retained for ~1 Gyr with respect to impact gardening on the trailing side of Ganymede with far fewer rays being found on the leading side.

For a cumulative growth rate $\propto t^{0.45}$ (each new impact must first penetrate through old regolith) modeled from Apollo lunar core data (Morris 1978), the average regolith thickness on Europa is then about 1 m in $t \sim 10^7$ years. However, there is little data on the growth rate at much smaller depths of centimeters to micrometers. The cumulative growth is driven by an initial rate $g_0 = 1.2$ μm year^{-1} due to the incident mass flux (Section 6.4) and an average mass ejection yield of 3×10^4 for icy surfaces as per Cuzzi and Estrada (1998). One expression fitting these combined constraints for the regolith depth D at time t in years is

$$D(t) = g_0\, t\left(1 + t \cdot t_0^{-1}\right)^{-0.55}\ [\mu\text{m}] \qquad (3)$$

for mixing time scale $t_0 = 1.7 \times 10^5$ years, but the sparseness of data allows other representations.

The meteoritic impacts laterally distribute ice mass within a few crater radii of the impact sites faster than it can be more globally distributed by sputtering and sublimation. Since the impact ejecta generally retain the molecular composition of the local material at the impact site, there is little change in regional brightness as also concluded by Spencer (1987a). *However, we also note that materials being processed by irradiation on short time scales (Section 5.1, Fig. 11) are buried faster by impact ejecta than are removed by sputtering or sublimation.* Some fraction of the buried products are thereby protected from decomposition (Section 9.3) by further irradiation.

8.4. Other Instabilities

Evidence for large-scale instabilities potentially driving vertical transport exists to varying degrees on all three satellites. The paucity of large impact craters on Europa suggests a downward collapse of such structures through a thin ice crust after formation. Thermal collapse of crater structures also occurs on Ganymede's surface, younger by several billions of years (Section 1.1) than that of Callisto. Relative absence on Callisto of small (<10-km) craters, smoothness of terrain imaged at highest resolution, and rim wall degradation for large craters indicates surface instabilities possibly created by radiation degradation of material, discussed here. Another possibility is upward leakage and sublimation of volatile gases (Moore *et al.* 1999), likely the detected CO_2 (Carlson 1999), from mantle degassing (Kargel *et al.* 2000) or the sub-surface ocean presently inferred from magnetic field data (Section 4.1).

9. CHEMICAL PROCESSING

9.1. General

Radiation doses are extremely high in the optical layers of all three satellites over the respective resurfacing timescales of ~10^7–10^9 years as evident from Fig. 11. Any material in the optical layer not sputtered away by the radiation, or otherwise depleted by thermal sublimation, is heavily processed even in geologically young areas (<10^7 years). Therefore, chemical evolution of the optical layers is dominated by particle and UV irradiation. Lower particle fluxes at Ganymede, particularly in the equatorial zone, and at Callisto are partly offset by the far longer

resurfacing times of those satellites. Thermal segregation effects may indeed dominate the optical reflectance of Ganymede and Callisto, as per Spencer (1987a), but the cumulative chemical effects of irradiation will be significant.

The ratios of the observed column densities to the computed source rates are determined by lifetime in the visible layer due to destruction, removal by sputtering or sublimation, and by dilution from meteoritic gardening (Section 8.3). For the latter reason, many (if not most) of the produced irradiation products are likely below this layer and are relatively protected from destruction by external irradiation. Measured column densities may only be lower limits, while production rates integrated over surface ages 10^7 to 10^9 years give upper limits for total column densities within and below the visible layer.

9.2. *Production of O_2, H_2 O_2, and CO_2*

Irradiation yield. Production of any particular species for a given dosage is often expressed by the yield factor G_X, the fractional number of product atoms or molecules of type X per 100 eV of deposited electronic energy (Johnson 1990, p. 93). G values must be used with caution as they can vary significantly with particle type and energy. In Fig. 15 we show the column densities produced over 1 year to depths up to 1 g cm^{-2} in each satellite region for unit values of G_X. Multiplication of these column densities by the actual yield G_X for a given irradiation product, and by a cumulative dose time t in years, gives the predicted column densities integrated to selected depths for comparison to available observations.

For O_2 some early experiments on radiation chemistry (Lefort 1955) give $G_{O_2} \sim 0.15$ for ionization energy loss in ice at 77 K.

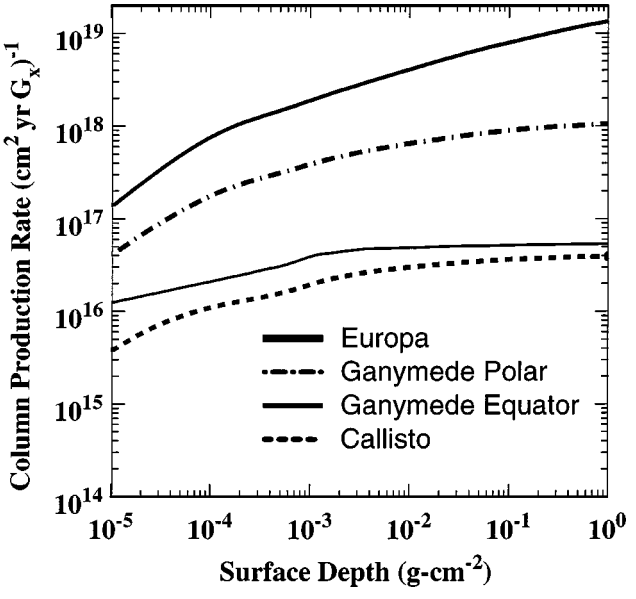

FIG. 15. Column density accumulated per year above depth shown for irradiation product X from $G_X = 1$ (Section 9.2) and pure H_2O ice on surfaces of Europa, Ganymede (polar cap and equator), and Callisto.

This result was obtained by melting the irradiated ice. Contamination by trapped atmospheric O_2 or CO_2 was thought to be low but possibly was not. More recent experiments (Vidal *et al.* 1997, Baragiola and Bahr 1998) suggest varied but lower O_2 yields. Baragiola *et al.* (1999) report only small upper limits for direct production of trapped O_2 within ice by 60 keV O_2^+ ($G_{O_2} < 5 \times 10^{-4}$) and 100 keV H^+ ($G_{O_2} < 4 \times 10^{-5}$), but higher yields are possible (Johnson 1999). For instance, $G_{O_2} \sim 0.01$ is obtained from other cross section data for O_2 sputtering from low energy electrons impacting thin ice films (Brown *et al.* 1982, Sieger *et al.* 1998). The electron-impact production of O_2 has a threshold energy of ~10 eV and requires the formation of stable precursors, possibly HO_2 or H_2O_2, before formation of O_2 by further electronic excitation. An additional O_2 source is also provided by irradiation of silicates or of hydrated salts (Hennig *et al.* 1953) in observed nonice materials on all three icy satellites (McCord *et al.* 1998b, 1999).

For the observed H_2O_2 on Europa, Carlson *et al.* (1999b) used $G \sim 0.4$ from Cottin and Lefort (1955) to estimate the production rate. The recent work of Moore and Hudson (2000) gives $G \sim 0.1$ to 0.4 in the presence of O_2 or CO_2 at 80 K but no detectable production for pure H_2O ice except at much lower temperature of ~20 K. The yield is enhanced in the presence of electron scavengers (see below) limiting the electron dissociation of produced H_2O_2.

The very tenuous CO_2 atmosphere on Callisto may arise from irradiation of nonice material on the surface. The observed CO_2 column density is $\sim 10^{15}$ cm^{-2} (Carlson 1999) and the inferred CO_2 source rate balancing dissociation losses from UV and particle irradiation is $\sim 6 \times 10^6$ cm^2 s^{-1}. Our calculated total energy flux in Table II would then only require a modest yield $G_{CO_2} \sim 3 \times 10^{-3}$ for ice heavily mixed with carbonaceous compounds if other sources are not available.

Losses. In the dark mottled terrain on the trailing hemisphere, scavaging by sulfur (Carlson *et al.* 1999a) might reduce the oxygen abundance below detectable levels. Oxidation of nonice materials within the ice crust below the surface may also decrease total O_2. However, the SO_2, sulfuric acid, and sulfate salts (e.g., $Na_2SO_4 \cdot nH_2O$) can also protect the H_2O_2 from dissociation by scavaging of free electrons (Ershov and Pikaev 1969) as also evidently occurs for $H_2O + CO_2$ mixtures (Moore and Hudson 2000). Carbon cycling in an H_2O matrix driven by irradiation may convert CO_2 to carbonic acid or another carbonate (Section 9.3) on reaction with buried nonice materials.

The surface irradiation environment also contributes to loss of O_2 and other associated irradiation products. Carlson *et al.* (1999b) found that the observed H_2O_2 abundance within the optical layer to depths $\leq$500 μm was consistent with equilibrium between production by energetic particles and dissociation by those same particles in ~100 days and by UV photons in ~four days. Sharp falloff in particle and UV fluxes at greater depths, and effects of meteoritic mixing (Section 8.3), could protect H_2O_2 and O_2 from dissociation for much longer periods of time.

9.3. Molecular Decomposition and Production of Other Volatiles

Hydrated minerals in dark surface regions would decompose under irradiation to produce SO_2, CO_2, and Na (Johnson *et al.* 1998, Johnson 2000a,b). Johnson (2000a,b) reviewed the efficient decomposition of sodium nitrate ($NaNO_3$) and carbonate (Na_2CO_3) under lightly ionizing radiation, but he also noted that the sulfates (e.g., Na_2SO_4) are much more stable, first losing water of hydration if irradiated in vacuum. The irradiated crystals can change color when dehydrated, but the original color reappears on subsequent exposure to water vapor. In the case of initially clear or white salt crystals this might account for brightening of originally dark terrain on Europa over time.

The sodium salts decompose under heavy ion bombardment, and neutral Na atoms are the dominant ejecta, as recently reviewed by Johnson (2000a), who proposed an Na component of the satellite atmospheres as detected on Europa (Brown and Hill 1996). Residual products left on the satellite surfaces for spectroscopic detection might include Na_2O, NaO, and NaS (Johnson 2000b). Also, lost Na atoms from Na_2SO_4 may be replaced by H, since sulfate bonds are strong (Johnson 2000b). This is one reason that Carlson *et al.* (1999a) suggested that the optical layer on Europa is dominated by hydrated sulfuric acid ($H_2SO_4 \cdot nH_2O$). For the magnesium salt hydrates such as $MgSO_4 \cdot 7H_2O$, more commonly known as epsom salt, Mg is less easily ejected than Na as measured in the gas phase (Johnson 2000a), so surface decomposition may lead to MgO, $Mg(OH)_2$, and other such compounds.

Carbon dioxide is a likely decomposition product of many organic molecules (e.g., Calvert and Pitts 1966) including the hydrated carbonates (e.g., natron, $Na_2CO_3 \cdot 10H_2O$) inferred by McCord *et al.* (1998a,b, 1999), while SO_2 can come from sulfate decomposition. CO_2 has been identified at Europa in association with the dark disrupted terrain of the trailing hemisphere where surface extrusions from endogenic sources seem likely. The observed SO_2-like absorption in UV data is often correlated to potential sites of sub-surface extrusions on Europa (Hendrix 1998). Internal degassing from the satellite mantles could provide major sources of CO_2 and SO_2 (Kargel *et al.* 2000) but would not directly account for hemispherical asymmetries of the observed surface abundances. Presence of CO_2 on Callisto's trailing hemisphere (McCord *et al.* 1998b) appears correlated to higher irradiation rates from corotating hot plasma ions but production from carbonate radiolysis seems unlikely (but see below) in the presumed absence of significant geologic sources for the carbonates.

Chemical decomposition of nonice materials could also be produced by acidic products of irradiation in a highly oxidizing surface environment. The known H_2O_2 and SO_2 in the europan surface ice and the sulfur radiolysis cycle proposed by Carlson *et al.* (1999a) naturally lead to the H_2SO_4 hydrate. A small abundance of about 1% of SO_2 and polymerized sulfur, relative to H_2SO_4, account in their work for UV absorption and spectral reddening features previously identified on Europa's trailing hemisphere. The C≡N component of hydrocyanic acid or hydrogen cyanide (HCN) is already a candidate for the 4.57-μm absorption feature in near-infrared imaging of the icy Galilean satellites (McCord *et al.* 1997, 1998b). Carbonic acid (H_2CO_3) persists as a stable product, even after heating to 200 K, when low-temperature ices containing CO_2 are irradiated (Moore and Khanna 1991, DelloRusso *et al.* 1993). Interactions of yet-unobserved H_2CO_3 with other hydrates in a radiation-driven carbon cycle might produce an *in situ* source of carbonates and the observed CO_2 (McCord *et al.* 1998b, Carlson 1999), even on the ancient surface of Callisto.

9.4. Molecular Synthesis

The Miller-Urey experiment (Miller 1953) demonstrated that complex chemical compounds of interest for astrochemistry and astrobiology can evolve from addition of energy (lightning, UV, energetic particles) to mixtures of abundant astrophysical molecules. These mixtures may start with simple molecules such H_2, H_2O, NH_3, CH_4, CO, and CO_2, yielding more complex species after long-term or intense irradiation. Polymerization of material in astrophysical ices has been commonly observed in later laboratory experiments after heavy irradiation by energetic ions (e.g., Strazzulla and Johnson 1991). Moore *et al.* (1991) irradiated mixtures of H_2O ice with CO and CO_2 to produce CH_3OH (methanol), H_2CO (formaldehyde), C_2H_5OH (ethanol), and CH_4. Formation of H_2CO_3 was discussed above (Section 9.3). Irradiation of CH_3OH in water ice leads in turn to $(CH_2OH)_2$, ethylene glycol, on warming from initial temperatures $T < 20$ to 200 K (Moore *et al.* 1996).

Moore and Donn (1982), Moore *et al.* (1983), and Khare *et al.* (1989) noted the presence of more complex hydrocarbons (e.g., long-chain polymers) in warmed residues of irradiated ices containing H_2O and CH_4. Some recent experiments with similar findings have been reported by Berstein *et al.* (1997) and by Strazzulla and Palumbo (1998). Hudson and Moore (1999) found that irradiation of only $H_2O + CO$ did not form such complex species, so initial composition of the ice appears to be important. Berstein *et al.* (1999) note that polycyclic aromatic hydrocarbons (PAHs) account for about 20% of interstellar carbon, accreting into Solar System bodies, and that UV irradiation of the PAHs in water ice produces various organic compounds of astrobiological interest. The production of such compounds may therefore arise from energetic particle and UV irradiation of a combination of primordial material and intermediate products of irradiation.

10. SUMMARY AND DISCUSSION

10.1. Overview of Results

In this paper we have calculated flux and energy inputs (Sections 2–6, Table II) of measured energetic particles in the

jovian magnetosphere on the surfaces of Europa, Ganymede, and Callisto. Improved instrumental discrimination between protons and ions (Section 2) and good agreement of electron flux spectra to the new measurements at sub-megaelectron volt energies, has allowed us to separate the effects of these different particle types for computations (Section 5) of sputtering, implantation, and of energy deposition as a function of depth. In the special case of Ganymede the energetic particle access to the surface has been modeled for the first time in terms of Størmer theory and numerical solutions for particle motions in the combined magnetospheric and satellite magnetic fields (Section 4). Except in the magnetically shielded region near Ganymede's equator, the energetic electrons (extended in our model data to energies of 1–40 MeV) are found to be the dominant carriers of energy for chemical radiolysis with decreasingly smaller relative inputs from protons and the heavy ions. The heavy ions likely dominate surface erosion through sputtering. In Ganymede's equatorial region the high mass-to-charge ratios of the heavy ions allow preferential access of these ions to the surface. Jovian energetic electrons above tens of kiloelectron volts are completely excluded from this region, while $\geq$10-MeV protons can penetrate but are lower in relative intensity, energy flux, and sputtering rate (Table II).

Magnitudes of the energetic particle effects have been compared (Sections 6 and 7) to those from solar UV photons, ENAs from the Io torus, micrometeorite impacts, thermal sublimation and annealing, and sub-surface heating from tidal interactions and radioisotope decay. Micrometeoroid and ENA impacts are found to deliver very negligible amounts of kinetic energy $\sim 10^5$ keV (cm^2-s)$^{-1}$ for chemical modification of the surfaces as compared to energy fluxes of $\leq 10^{11}$ keV (cm^2-s)$^{-1}$ from magnetospheric particle irradiation. While the elemental composition of each satellite surface arises mostly from endogenic materials, the relatively large energy inputs from irradiation should evolve the observable *molecular* chemistry (Section 9) everywhere on short timescales (Section 8.1, Fig. 11), a few years in the case of material at micrometer depths on Europa to thousands of years at the same depths on Callisto. Even the 10^3 to 10^6 year times for full radiation processing throughout the millimeter-thick optical layers of each satellite surface region are very short as compared to the 10^7- to 10^9-year geological ages of those surfaces.

While solar photons provide the largest gross source of energy, as at Earth, the most chemically significant input from UV-C (Table III) is overwhelmed in the case of Europa by that from the energetic particles (Section 6). The latter is even comparable to tidal energy dissipation to heat within Europa and may contribute to interior heating by oxidation of carbonaceous irradiation products conveyed to a sub-surface ocean via instabilities of the overlying ice crust. Long-term survival and initial downward migration of these and other irradiation products should be enhanced by meteoritic burial to millimeter depths over 10^3 years and to meter depths over 10^7 years (Section 8.3).

As earlier proposed by Spencer (1987a) from Voyager-era observations, surface distributions for visibly bright ices are inferred here (Section 8.2) to be controlled by ion sputtering or radiation damage at Europa and at Ganymede's poles, and by thermal segregation in Ganymede's equatorial regions and on Callisto. However, we also find that meteoritic gardening effects may be especially important with respect to interpretation of abundance from remote sensing observations for apparent irradiation products (e.g., SO_2, H_2O_2, O_2, CO_2). Inferred column densities may only be lower limits to total abundance integrated in and below the optical layer.

10.2. State of Energetic Particle Measurements and Models

Our energetic particle measurements are taken from the early Galileo Orbiter encounters with the three icy satellites and are somewhat biased by the spatial locations of these encounters within the jovian magnetosphere and with respect to vertical offset from the plasma current sheet (Section 2.2). Future work will address spatial and temporal variations during later encounters of the primary Galileo Orbiter mission (1995–1997), the Galileo Europa Mission (1997–1999), and the now ongoing Galileo Millennium Mission. Our comparison to energy fluxes near Europa orbit from Voyager LECP data shows no temporal variability, but order of magnitude variations could have occurred further out and been obscured by spatial differences in the measurements. Some differences could simply be due to improved elemental resolution.

In this work we did not model effects of complex and varying magnetic field configurations. Størmer energy cutoffs for an axisymmetric dipole field around Ganymede are easily computed for our assumed (Section 2.3) ion charge states (H^+, O^{2+}, S^{3+}), but the time-varying external and induced fields (Section 4.1) require averaging for different orientations of the external magnetospheric field during orbital motion of the satellites around Jupiter. More definitive models must also allow for magnetic field contributions from plasma currents and ionospheric coupling within the satellite magnetospheres. Pending availability of such models, we have chosen (Sections 4.2–4.3) the simplest possible representations: (1) no internal or induced field at all for Europa and Callisto and (2) a simple dipole aligned to the local jovian magnetospheric field direction for Ganymede.

Finally, the values we compute for irradiation parameters (Section 5) are equivalent to global averages over the surface of each satellite, except that values for Ganymede are separately computed for the equatorial and polar cap regions. The incident particle spectra are taken to be those upstream of each satellite with respect to corotation with the planetary magnetic field, the downstream depletion by satellite sweeping being ignored. For particles with gyroradii much less than the satellite radius (Section 3.3, Fig. 4), maximum impact fluxes are expected on the trailing hemisphere where our global estimates are therefore a factor of two or more lower than the local irradiation rates.

10.3. Relevance to Surface Composition

All telescopic measurements to date have made spectroscopic observations for compositional analyses of the satellite surfaces

as "through a glass, darkly." Other than on Io, fresh plumes of sub-surface ejecta revealing compositions of the interiors have yet to be detected. The previously cited detection of CO_2 on Callisto, O_2 and O_3 on Ganymede, and H_2O_2 on Europa are suggestive of irradiation processing of the surface (Sections 9.1–9.3). The recent report (Carlson *et al.* 1999a) of sulfur in the form of hydrated sulfuric acid on Europa is consistent with irradiation of sulfate salts (e.g., Na_2SO_4) in a water ice environment. In all cases we assume that molecular composition is largely driven by irradiation processes. Due to micrometeorite mixing of the materials in the surface regolith (Section 8.3), the time to accumulate a detectable column density is increased. However, this means that a large reservoir of undetected material may reside below the sensed layer. For this reason it would be highly desirable to probe the surface composition *in situ* to meter depths for irradiation products.

Even if the elemental and molecular sources of nonice materials are endogenic, as they now appear be on Europa (Fanale *et al.* 1999), the irradiation can expose and modify the nonice material beneath thin H_2O frost (Section 8.2). Simple correlation of SO_2 surface abundance, determined from UV spectroscopy, to iogenic sulfur implantation rates, is therefore unlikely. Longitude dependence and time variability of UV absorption spectra have been reported for all three satellites from IUE observations (Section 7.1) and are potentially explainable in terms of temporal and spatial variations in magnetospheric energy inputs (Section 7.2). While endogenic SO_2 excavated by meteoritic impacts seems a plausible source for UV absorption on Callisto's leading hemisphere (Lane *et al.* 1981), the concentration of CO_2 on the trailing hemisphere (McCord *et al.* 1998b) does suggest magnetospheric irradiation as an exogenic energy source. A trailing hemisphere enhancement of irradiation products can also be magnified by a higher rate of mixing (Section 8.3) below the optical layer from meteoritic impacts on the leading side.

In the case of Ganymede there are several outstanding puzzles related to oxygen and sulfur: (1) origin of "condensed" O_2 in the trailing low latitude regions (Calvin and Spencer 1997), (2) origin of the ozone-like feature detected (Hendrix *et al.* 1999) primarily at large solar zenith angles (e.g., high latitude near local noon, lower latitudes near dawn and dusk), and (3) enhanced UV absorption by SO_2 and O_2–O_3 abundances on the trailing hemisphere (Nelson *et al.* 1987, Calvin *et al.* 1995, Spencer *et al.* 1995, Noll *et al.* 1996, McCord *et al.* 1998b) despite shielding by the satellite's magnetic dipole field. Since magnetic shielding below 40° latitude reduces the production (Fig. 15), sublimation of H_2O followed by photochemical production may contribute. However, sputtering and transport can be driven by the heavy ions, which more easily penetrate the magnetic field at the low charge states (O^{2+}, S^{3+}) assumed here (Section 2.3). The O_2 may be preferentially removed from, or buried beneath, the optical layer on the leading hemisphere by micrometeoroid impacts (Calvin and Spencer 1997, Spencer 1998), thereby enhancing hemispherical differences. In addition, the weak "solid" O_2 absorption feature requires a long optical pathlength for detection, so its absence from the more reflective polar region of Ganymede, and globally on Europa, is not surprising. Concentrations in the trailing hemisphere may indicate direct access of low-energy electrons and low-energy (<10 keV) corotating plasma to the surface (Section 4.2 and Fig. 10).

We further expect that the magnetic dipole moment of Ganymede may have varied and even reversed, like the terrestrial and early martian (Connerney *et al.* 1999) magnetic fields, many times during the $\sim 10^9$ year surface age of that satellite. If so, the penetrating particle fluxes could have been much higher for thousands to millions of years, and a significant O_2 reservoir could then have accumulated in or under the surface. Preferential vapor deposition at mid-latitudes (Purves and Pilcher 1980, Shaya and Pilcher 1984), followed by thermal annealing (Johnson 1985, 1999), may have been sufficient to keep optical pathlengths long in the relatively dark material at low latitudes in long intervals between dipole reversals.

10.4. Astrobiological Implications

Habitable zone. We speculate on the debate about whether life might have evolved within the subsurface ocean of Europa. This is important for the general question of how often and where life might have arisen throughout the universe. If we accept the assumption of Gaidos *et al.* (1999), that biological processes are ultimately driven by solar energy through photosynthesis, then there appear to be few prospects for evolution of terrestrial life forms at Europa. The habitable zone for life in any stellar system is then narrowly restricted to solar irradiation environments and planetary histories similar to that of Earth. Alternatively, we argue with Chyba (2000) that irradiation production could supplant some photosynthetic resources for astrobiology. If we only require that there be water, hydrocarbons, and other chemicals needed for life, and sufficient interior heating (e.g., tidal, radiogenic, chemical) and related crustal activity to maintain vertical transport for biological resources and waste products, then the definition of habitable zone is greatly broadened.

Surface environment. Survival of any conceivable organisms at the surfaces of icy satellites is clearly limited in part by very low temperature and air pressure, leading to severe dehydration, and by the sterilizing irradiation environment. Depth profiles of volume dosage rates (megarad per month) from the measured energetic particles are shown in Fig. 16 by region for all three satellites. Note that significant chemical breakdown occurs at vastly greater dosages than required for lethality in terrestrial living organisms. The hardiest example of the latter may be the terrestrial bacterium *Deinococcus radiodurans*, which can survive ionizing radiation dosages up to 0.5 Mrad with little apparent effect (Battista 1997). Such organisms might survive on Europa's surface in a dormant state for several days or more at the base of the optical layer after ejection from sub-surface environments. At meter depths the surface ice would shield transient liquid water environments from rapid sterilization, and a deep ocean below kilometers of ice crust would be completely

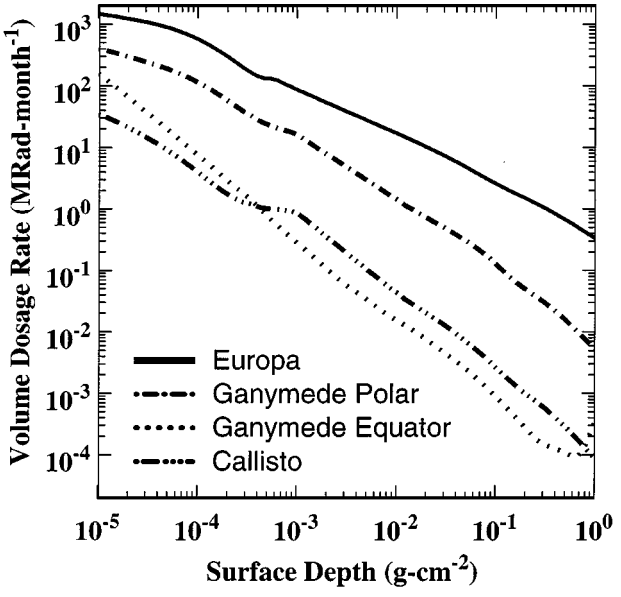

FIG. 16. Depth profiles for total volume dosage rate in megarad (Mrad) per month for irradiation of pure H_2O ice on surfaces of Europa, Ganymede (polar cap and equator), and Callisto. Note that 1 Mrad $= 10^4$ Grays $= 10^8$ erg cc^{-1} and that the chemical dose unit of 100 eV 16 amu^{-1} in Fig. 11 equals 6.03×10^4 Mrad.

protected. Future possibilities include *in situ* searches for biological material imbedded either in surface ice or in ice grains ejected into space by meteoroid impacts.

Chemical energy. Continuous energy input from irradiation, and preferential loss of hydrogen from the surface by sputtering of water ice (e.g., Johnson 1995), lead to an abundance of oxidants and other products of irradiation with high energy content. Much of the incident particle and UV energy may be retained within the irradiated layer and converted to chemical potential energy by the breaking and remaking of molecular bonds (Sections 9.2–9.4). While substantial amounts of the irradiation energy are likely dissipated in cyclic reactions, such as dissociation and recombination of H_2O, or else returned to the magnetosphere via sputtering and escape, the rest is stored in production of volatiles (O_2, CO_2), other oxidants such as peroxide, sulfates, and carbonates, and simple to complex hydrocarbons. Further reactions of these irradiation products will affect subsurface chemistry and also produce heat. Exothermic oxidation of hydrocarbons, including the irradiation products and primordial materials, could release heat, either via spontaneous combustion in high-pressure oxygen at the ice–liquid interface (see next subsection) or at 10^3 K temperatures in hydrothermal vent systems at the floor of the europan ocean. The 10^7-year recyling time of the europan ice crust is interestingly similar to the time for cycling of material through such systems in the terrestrial oceans (Miller and Bada 1988).

Surface gardening and geologic instabilities may convey resi dual irradiation products and their stored chemical energy through the outer kilometers of ice crust to subsurface environments. As discussed in Section 8.3, material at the irradiated surfaces can become buried within the regolith to meter depths by meteoritic impacts within the 10^7- to 10^9-year ages of these icy surfaces. At greater depths the ices in the satellites crusts may resemble Antarctic ices with an upper layer of "bubbly" ice overlaying a deeper layer containing clathrate hydrates (Miller 1969). Calvin *et al.* (1996) showed that Ganymede's lower temperatures and gravity, as compared to those of Earth, allow O_2 clathrate stability below centimeter depths near the poles and below 100-m depths near the dayside equator. As clathrates and other forms of the irradiation products reach the ice-liquid interface, chemical reactions releasing heat would likely be accelerated in the high-pressure environment under kilometers of ice crust. The rise in temperature from $\sim$100 K at the surface to $\leq$273 K at the liquid layer may itself drive many heat-producing reactions, as found from recent laboratory studies for astrophysical ice mixtures heated above 40 K (Woon 1999).

Oxygen. At upper limits on oxygen yields (Section 9.2), a substantial amount of O_2, equivalent to oxygenation levels in terrestrial oceans, is produced by irradiation of Europa's surface. For an electron energy flux of $\sim 5 \times 10^{10}$ keV (cm^2-s)$^{-1}$ (Table II), the O_2 source rate for H_2O ice irradiation at Europa with $G_{O_2} \sim 0.01$ is 5×10^9 O_2 (cm^2 s)$^{-1}$. This value may at least double on the trailing hemisphere. Ion bombardment gives a further contribution of $\leq 10^9$ O_2 (cm^2 s)$^{-1}$, dependent on plasma access to the surface (Sections 3.2 and 8.2), for a global average net source $\leq 10^{10}$ O_2 (cm^2 s)$^{-1}$. This source rate, ignoring all losses discussed above, would limit the net oxygen column to $\sim 3 \times 10^{24}$ O_2 cm^{-2} for during the 10^7-year resurfacing time of the ice crust. Less volatile oxidants are produced and trapped more efficiently. Chyba (2000) has noted that the observed H_2O_2 in the optical layer would provide an O_2 source for the Europan ocean after dissociation in liquid solution within 10 years. $G \sim 0.1$ for H_2O_2 (Section 9.2) would then ultimately give 10 times more O_2 than from the direct O_2 production above.

If a fraction of the produced oxidants are trapped in the surface material and then subducted by various geologic processes, then a significant supply of oxygen may be made available to the subsurface ocean. For a typical mass concentration $\leq$10 mg per liter from photosynthetically produced O_2 in the terrestrial ocean at depths down to 150 m (Schlesinger 1997), Europa's ocean could be fully oxygenated at this level throughout the *entire* depth of $\leq 10^2$ km from the direct O_2 product of surface irradiation. Additional contributions from H_2O_2 and other oxidants could increase the oxygenation level by up to an order of magnitude.

Pockets of compressed O_2 gas and other volatiles released from hydrates could form at the ice–liquid interface but might be toxic at high partial pressures to analogs of terrestrial life forms. Consumption of the O_2 in gas phase through combustion (see above) of carbonaceous materials in the melting ice, and in dissolved form within hydrothermal vent systems, might limit O_2 concentrations in the postulated air gap and ocean to levels

supporting life while also contributing heat for the Europa interior in addition to that from tidal effects. Lower production yields $G_{O_2} \ll 0.01$ at the surface, or large oxidant losses in transit from the irradiated surface to the ice–air–water interface, may also limit the O_2 concentrations.

Other planetary systems. Since the four large planets in our Solar System all have magnetospheres and many icy satellites, similar configurations may be expected in other planetary systems with detectable (but not yet directly observable) planets, and perhaps one satellite in each such system may be like Europa. Radio frequency searches for signatures of planetary magnetic fields would therefore be useful in systems with identified extrasolar planets (Farrell *et al.* 1999). Noll *et al.* (1997b) suggested that icy planets in high-radiation environments might produce false signals in astronomical searches for life through detection of O_3. This would mainly apply for observations restricted to ultraviolet wavelengths; infrared measurements provide limits on surface temperature for planetary objects. Here we speculate that the inverse may be true: *icy satellites and planets with significant heat, irradiation, and sub-surface water resources may provide common abodes for life throughout the universe*. Evolution of Earth-like life forms on planetary surfaces exposed to various potentially catastrophic hazards from the space environment (solar radiation, large asteroid and comet impacts, shock waves and cosmic rays from nearby super-novae, gamma rays from merger of binary neutron stars) may be comparably rare. Meteoritic ejecta from inhabited icy bodies could carry the biochemical seeds of life to other bodies. For these reasons Europa might therefore provide a more universal model for testing theories of astrobiological "origins" than Earth.

ACKNOWLEDGMENTS

We thank the EPD Principal Investigator, Don Williams of Applied Physics Laboratory–Johns Hopkins University, for permission to use EPD data in this study. W.-H. Ip of the Max Planck Institute for Aeronomy provided preliminary EPD ion spectra for Europa in advance of the Ip *et al.* (1997) publication. D. F. Smart and M. A. Shea of the former Air Force Geophysics Laboratory provided updated versions of their particle trajectory code for computations of Størmer cutoffs. The highly useful SRIM code of Ziegler *et al.* (1985) was obtained from the following IBM web site: http://www.research.ibm.com/ionbeams/. J. P. Wefel and T. G. Guzik of Louisiana State University provided J.F.C. with an original source code for calculations of energy deposition versus depth using other range and energy loss routines. Electron range data (Fig. 13) was supplied by A. J. Tuzzolino of the University of Chicago. M. Horányi from the University of Colorado provided useful insights on modeling of dust particle trajectories in the jovian system. R. Evans of the Jet Propulsion Laboratory provided data on dosage profiles of bremsstrahlung gamma rays, as discussed in Section 8.1, from a Europa electron spectrum similar to that in Fig. 1. We thank C. A. Hibbitts of the University of Hawaii for comments on the manuscript. J.F.C. was supported through Raytheon ITSS by NASA Contracts NAS5-97059 and NAS5-98156 for the SSDOO Project at Goddard Space Flight Center. He also appreciates new support from the Jovian System Data Analysis Program through NASA Contract NASW-99029. R.E.J. acknowledges a senior National Research Council fellowship at the Goddard Institute for Space Studies and support from NASA's Planetary Geology and Geophysics Program. H.B.G. was supported at the Jet Propulsion Laboratory by a NASA contract.

REFERENCES

Baragiola, R. A., and D. A. Bahr 1998. Laboratory studies of the optical reflectance and stability of oxygen on Ganymede. *J. Geophys. Res.* **103**, 25865–25872.

Baragiola, R. A., C. L. Atteberry, and D. A. Bahr 1999. Reply. *J. Geophys. Res.* **104**, 14183–14187.

Bar-Nun, A., G. Herman, M. L. Rappaport, and Y. Mekler 1985. Ejection of H_2O, O_2, H_2, and H from water ice by 0.5–6 keV H^+ and Ne^+ ion bombardment. *Surf. Sci.* **150**, 143–156.

Battista, J. R. 1997. AGAINST ALL ODDS: The survival strategies of Deinococcus radiodurans. *Annu. Rev. Microbiol.* **51**, 203–224.

Bell, E. V., II, and T. P. Armstrong 1986. Monte carlo simulation of charged particle impact on the satellites of Jupiter and Saturn. *J. Geophys. Res.* **91**, 1397–1403.

Belton, M. J. S., and 33 colleagues 1996. Galileo's first images of Jupiter and the Galilean satellites. *Science* **274**, 377–385.

Berstein, M. P., L. J. Allamandola, and S. A. Sanford 1997. Complex organics in laboratory simulations of interstellar/cometary ices. *Adv. Space Res.* **19**, 991–998.

Berstein, M. P., S. A. Sanford, L. J. Allamandola, J. S. Gillette, S. J. Clemett, and R. A. Zare 1999. UV irradiation of polycyclic aromatic hydrocarbons in ices: Production of alcohols, quinones, and ethers. *Science* **283**, 1135–1138.

Bridge, H. S., and 11 colleagues 1979. Plasma observations near Jupiter: Initial results from Voyager 1. *Science* **204**, 987–991.

Brown, M. E., and R. E. Hill 1996. Discovery of an extended sodium atmosphere around Europa. *Nature* **380**, 229–231.

Brown, W. L., W. M. Augustyniak, E. Simmons, K. J. Marcatanio, L. J. Lanzerotti, R. E. Johnson, J. W. Boring, C. T. Reimann, G. Foti, and V. Pirronello 1982. Erosion and molecule formation in condensed gas films by electronic energy loss of fast ions. *Nuclear Instrum. Methods* **198**, 1–8.

Burns, J. A., M. R. Showalter, D. P. Hamilton, P. D. Nicholson, I. de Pater, M. Ockert-Bell, and P. C. Thomas 1999. The formation of Jupiter's faint rings. *Science* **284**, 1146–1150.

Calvert, J. G., and J. N. Pitts 1966. *Photochemistry*. Wiley, New York.

Calvin, W., and J. R. Spencer 1997. Latitudinal distribution of O_2 on Ganymede: Observations with the Hubble Space Telescope. *Icarus* **130**, 505–516.

Calvin, W. M., R. N. Clark, R. H. Brown, and J. R. Spencer 1995. Spectra of the icy Galilean satellites from 0.2 to 5 μm: A compilation, new observations, and a recent summary. *J. Geophys. Res.* **100**, 19041–19048.

Calvin, W. M., R. E. Johnson, and J. R. Spencer 1996. O_2 on Ganymede: Spectral characteristics and plasma formation mechanisms. *Geophys. Res. Lett.* **23**, 673–676.

Carlson, R. W. 1999. A tenuous carbon dioxide atmosphere on Jupiter's moon Callisto. *Science* **283**, 820–821.

Carlson, R. W., R. E. Johnson, and M. S. Anderson 1999a. Sulfuric acid on Europa and the radiolytic sulfur cycle. *Science* **286**, 97–99.

Carlson, R., and 13 colleagues 1999b. Hydrogen peroxide on the surface of Europa. *Science* **283**, 2062–2064.

Carr, M. H., M. J. S. Belton, C. R. Chapman, M. E. Davies, P. Geissler, R. Greenberg, A. S. McEwen, B. R. Tuffs, R. Greeley, and R. Sullivan 1998. Evidence for a subsurface ocean on Europa. *Nature* **391**, 363–365.

Cassen, P., S. J. Peale, and R. T. Reynolds 1980. On the comparative evolution of Ganymede and Callisto. *Icarus* **41**, 232–239.

Cassen, P., R. T. Reynolds, and S. J. Peale 1979. Is there liquid water on Europa? *Geophys. Res. Lett.* **6**, 731–734.

Chyba, C. F. 2000. Energy for microbial life on Europa. *Nature* **403**, 381–382.

Collier, M. R., and D. C. Hamilton 1995. The relationship between kappa and temperature in energetic ion spectra at Jupiter. *Geophys. Res. Lett.* **22**, 303–306.

Connerney, J. E. P., M. H. Acuña, P. J. Wasilewski, N. F. Ness, H. Rème, C. Mazelle, D. Vignes, R. P. Lin, D. L. Mitchell, and P. A. Cloutier 1999. Magnetic lineations in the ancient crust of Mars. *Science* **284**, 794–798.

Cooper, J. F. 1983. Nuclear cascades in Saturn's rings: Cosmic ray albedo neutron decay and origins of trapped protons in the inner magnetosphere. *J. Geophys. Res.* **88**, 3945–3954.

Cooper, J. F., and E. V. Bell II 1999. Energy cutoffs for penetration of Jovian energetic particles to the surface of Ganymede through the satellite's magnetic field environment. *Eos Trans. AGU, 1999 Spring Meet. Suppl.* **80**, S301.

Cooper, J. F., and J. A. Simpson 1980. Sources of high-energy protons in Saturn's magnetosphere. *J. Geophys. Res.* **85**, 5793–5802.

Cooper, J. F., J. H. Eraker, and J. A. Simpson 1985. The secondary radiation under Saturn's A–B–C rings produced by cosmic ray interactions. *J. Geophys. Res.* **90**, 3415–3427.

Cooper, J. F., N. Gehrels, R. E. Johnson, C. M. Cohen, and N. Murphy 1997a. Energetic ion irradiation of the Galilean satellites. *Eos Trans. AGU 1997 Spring Meeting Suppl.* **78**, S307.

Cooper, J. F., B. H. Mauk, C. M. Cohen, R. E. Johnson, and N. Gehrels 1997b. Irradiation of icy Galilean satellites by energetic ions: Calculations derived from Galileo EPD and HIC flux spectra. *Eos Trans. AGU 1997 Fall Meeting Suppl.* **78**, F418.

Cottin, M., and M. Lefort 1995. Sur le mécanisme chimque primaire de radiolyse and de L' eau, *J. Chim. Phys.* **52**, 545–555.

Crary, F. J., F. Bagenal, L. A. Frank, and W. R. Paterson 1998. Galileo plasma spectrometer measurements of composition and temperature in the Io plasma torus. *J. Geophys. Res.* **103**, 29359–29370.

Cuzzi, J. N., and P. R. Estrada 1998. Compositional evolution of Saturn's rings due to meteoroid bombardment. *Icarus* **132**, 1–35.

Delitsky, M. L., and A. L. Lane 1998. Ice chemistry on the Galilean satellites. *J. Geophys. Res.* **103**, 31391–31403.

DelloRusso, N., R. K. Khanna, and M. H. Moore 1993. Identification and yield of carbonic acid and formaldehyde in irradiated ices. *J. Geophys. Res.* **98**, 5505–5510.

Divine, N., and H. B. Garrett 1983. Charged particle distributions in Jupiter's magnetosphere. *J. Geophys. Res.* **88**, 6889–6903.

Domingue, D. L., and A. L. Lane 1998. IUE views Europa: Temporal variations in the UV. *Geophys. Res. Lett.* **25**, 4421–4424.

Domingue, D. L., A. L. Lane, and R. A. Beyer 1998. IUE's detection of tenuous SO_2 frost on Ganymede and its rapid time variability. *Geophys. Res. Lett.* **25**, 3177–3120.

Draganić, I. G., Z. D. Draganić, and S. Vujošević 1984. Some radiation-chemical aspects of chemistry in cometary nuclei. *Icarus* **60**, 464–475.

Ershov, S. G., and A. K. Pikaev 1969. Stabilized free radicals in the radiation chemistry of frozen aqueous systems. *Radiation Res. Rev.* **2**, 1–101.

Eviatar, A., and D. A. Barbosa 1984. Jovian magnetospheric neutral wind and auroral precipitation flux. *J. Geophys. Res.* **89**, 7393–7398.

Farrell, W. M., M. D. Desch, and P. Zarka 1999. On the possibility of coherent cyclotron emission from extrasolar planets. *J. Geophys. Res.* **104**, 14025–14032.

Fanale, F. P., and 22 colleagues, The Galileo NIMS, SSI, UVS instrument teams 1999. Galileo's multiinstrument spectral view of Europa's surface composition. *Icarus* **139**, 179–188.

Fillius, W. 1988. Toward a comprehensive theory for the sweeping of trapped radiation by inert orbiting matter. *J. Geophys. Res.* **93**, 14284–14294.

Frank, L. A., W. R. Paterson, K. L. Ackerson, V. M. Vasyliunas, F. V. Coroniti, and S. J. Bolton 1996. Plasma observations at Io with the Galileo spacecraft. *Science* **274**, 394–395.

Frank, L. A., W. R. Paterson, K. L. Ackerson, and S. J. Bolton 1997. Low-energy electron measurements at Ganymede with the Galileo spacecraft: Probes of the magnetic topology. *Geophys. Res. Lett.* **24**, 2159–2162.

Gaidos, E. J., K. H. Nealson, and J. L. Kirschvink 1999. Life in ice-covered oceans. *Science* **284**, 1631–1633.

Geiss, J., G. Gloeckler, H. Balsiger, L. A. Fisk, A. B. Galvin, F. Gliem, D. C. Hamilton, F. M. Ipavich, S. Livi, and U. Mall 1992. Plasma composition results in Jupiter's magnetosphere: Initial results from the Solar Wind Ion Composition Spectrometer. *Science* **257**, 1535–1539.

Grundy, W. M., M. W. Buie, J. A. Stansberry, J. R. Spencer, and B. Schmitt 1999. Near-infrared spectra of icy outer solar system surfaces: Remote determination of H_2O ice temperatures. *Icarus* **142**, 536–549.

Hall, L. A., L. J. Heroux, and H. E. Hinterregger 1985. Solar ultraviolet irradiance. In *Handbook of Geophysics and the Space Environment* (A. S. Jura, Ed.), pp. 2-1–2-21. Air Force Geophysics Laboratory, Hanscom AFB, MA.

Hamilton, D. C., G. Gloeckler, S. M. Krimigis, and L. J. Lanzerotti 1981. Composition of nonthermal ions in the jovian magnetosphere. *J. Geophys. Res.* **86**, 8301–8318.

Hendrix, A. R. 1998. Galileo UVS observations of Europa: Variations in ultraviolet absorber with surface features. *Eos Trans. AGU Fall Meet. Suppl.* **79**(45), F537.

Hendrix, A. R., C. A. Barth, and C. W. Hord 1999. Ganymede's ozone-like absorber: Observations by the Galileo ultraviolet spectrometer. *J. Geophys. Res.* **104**, 14169–14178.

Hennig, G., R. Lees, and M. S. Matheson 1953. The decomposition of nitrate crystals by ionizing radiations, *J. Chem. Phys.* **21**, 664–668.

Hudson, R. L., and M. H. Moore 1999. Laboratory studies of the formation of methanol and other organic molecules by water + carbon monoxide radiolysis: Relevance to comets, icy satellites, and interstellar ices. *Icarus* **140**, 451–461.

Ip, W.-H., D. J. Williams, R. W. McEntire, and B. Mauk 1997. Energetic ion sputtering effects at Ganymede. *Geophys. Res. Lett.* **24**, 2631–2634.

Ip, W.-H., D. J. Williams, R. W. McEntire, and B. H. Mauk 1998. Ion sputtering and surface erosion at Europa. *Geophys. Res. Lett.* **25**, 829–832.

Johnson, R. E. 1985. Polar frost formation on Ganymede. *Icarus* **62**, 344–347.

Johnson, R. E. 1990. *Energetic Charged Particle Interactions with Atmospheres and Surfaces.* Springer-Verlag, Heidelberg.

Johnson, R. E. 1995. Sputtering of ices in the outer Solar System. *Rev. Mod. Phys.* **68**, 305–312.

Johnson, R. E. 1997. Polar "caps" on Ganymede and Io revisited. *Icarus* **128**, 469–471.

Johnson, R. E. 1998. Sputtering and desorption from icy surfaces. In *Solar System Ices* (B. Schmitt, C. de Bergh, and M. Festou, Eds.), pp. 303–334. Kluwer Academic, Netherlands.

Johnson, R. E. 1999. Comment on "Laboratory studies of the optical properties and stability of oxygen on Ganymede" by Raul A. Baragiola and David A. Bahr." *J. Geophys. Res.* **104**, 14179–14182.

Johnson, R. E. 2000a. Sodium at Europa. *Icarus* **143**, 429–433.

Johnson, R. E. 2000b. Surface chemistry in the jovian magnetosphere radiation environment. In *Chemical Dynamics in Extreme Environments* (R. Dressler, Ed.), Advanced Series in Physical Chemistry, World Scientific, in press.

Johnson, R. E., and T. I. Quickenden 1997. Photolysis and radiolysis of water ice on outer Solar System bodies. *J. Geophys. Res.* **102**, 10985–10996.

Johnson, R. E., J. W. Boring, C. T. Reimann, L. A. Barton, E. M. Sieveka, J. W. Garrett, K. R. Farmer, W. L. Brown, and L. J. Lanzerotti 1983. Plasma ion-induced molecular ejection on the Galilean satellites: Energies of ejected molecules. *Geophys. Res. Lett.* **10**, 892–895.

Johnson, R. E., J. F. Cooper, L. J. Lanzerotti, and G. Strazzulla 1987. Radiation formation of a non-volatile crust. *Astron. Astrophys.* **187**, 889–892.

Johnson, R. E., R. M. Killen, J. H. Waite, Jr., and W. S. Lewis 1998. Europa's surface composition and sputter-produced ionosphere. *Geophys. Res. Lett.* **25**, 3257–3260.

Kane, M., B. H. Mauk, E. P. Keath, and S. M. Krimigis 1995. Hot ions in Jupiter's magnetodisc: A model for Voyager 2 low-energy charged particle measurements. *J. Geophys. Res.* **100**, 19473–19486.

Kargel, J. S., J. Kaye, J. W. Head III, G. Marion, R. Sassen, J. Crowley, O. Prieto, S. Grant, and D. Hogenboom 2000. Europa's crust and ocean: Origin, composition, and the prospects of life. *Icarus* **148**, 226–265.

Keppler, E., and N. Krupp 1996. The charge state of helium in the jovian magnetosphere: Possible method to determine it. *Planet. Space Sci.* **44**, 71–75.

Khare, B. N., W. R. Thompson, B. G. J. P. T. Murray, C. F. Chyba, and C. Sagan 1989. Solid organic residues produced by irradiation of hydrocarbon-containing H_2O and H_2O/NH_3 ices: Infrared spectroscopy and astronomical implications. *Icarus* **79**, 350–361.

Khurana, K. K. 1997. Euler potential models of Jupiter's magnetospheric field. *J. Geophys. Res.* **102**, 11295–11306.

Khurana, K. K., M. G. Kivelson, C. T. Russell, R. J. Walker, and D. J. Southwood 1997. Absence of an internal magnetic field at Callisto. *Nature* **387**, 262–264.

Khurana, K. K., M. G. Kivelson, D. J. Stevenson, G. Schubert, C. T. Russell, R. J. Walker, and C. Polanskey 1998. Induced magnetic fields as evidence for subsurface oceans in Europa and Callisto. *Nature* **395**, 777–780.

Kivelson, M. G., K. K. Khurana, F. V. Coroniti, S. Joy, C. T. Russell, R. J. Walker, J. Warnecke, L. Bennett, and C. Polanskey 1997a. The magnetic field and magnetosphere of Ganymede. *Geophys. Res. Lett.* **24**, 2155–2158.

Kivelson, M. G., K. K. Khurana, S. Joy, C. T. Russell, D. J. Southwood, R. J. Walker, and C. Polanskey 1997b. Europa's magnetic signature: Report from Galileo's pass on 19 December 1996. *Science* **276**, 1239–1241.

Kivelson, M. G., K. K. Khurana, C. T. Russell, R. J. Walker, J. Warnecke, F. V. Coroniti, C. Polanskey, D. J. Southwood, and G. Schubert 1996. Discovery of Ganymede's magnetic field by the Galileo spacecraft. *Nature* **384**, 537–541.

Kivelson, M. G., K. K. Khurana, D. J. Stevenson, L. Bennett, S. Joy, C. T. Russell, R. J. Walker, C. Zimmer, and C. Polanskey 1999. Europa and Callisto: Induced or intrinsic fields in a periodically varying plasma environment. *J. Geophys. Res.* **104**, 4609–4625.

Krimigis, S. M., T. P. Armstrong, W. I. Axford, C. O. Bostrom, C. Y. Fan, G. Gloeckler, and L. J. Lanzerotti 1977. The Low Energy Charged Particle (LECP) experiment on the Voyager spacecraft. *Space Sci. Rev.* **21**, 329–354.

Krimigis, S. M., T. P. Armstrong, W. I. Axford, C. O. Bostrom, C. Y. Fan, G. Gloeckler, L. J. Lanzerotti, E. P. Keath, R. D. Zwickl, J. F. Carbary, and D. C. Hamilton 1979. Low energy charged particle environment at Jupiter—A first look. *Science* **204**, 998–1003.

Krüger, H., A. V. Krivov, D. P. Hamilton, and E. Grün 1999. Detection of an impact-generated dust cloud around Ganymede. *Nature* **399**, 558–560.

Lane, A. L., and D. L. Domingue 1997. IUE's view of Callisto: Detection of an SO_2 absorption correlated to possible torus neutral wind alterations. *Geophys. Res. Lett.* **24**, 1143–1146.

Lane, A. L., R. M. Nelson, and D. L. Matson 1981. Evidence for sulfur implantation in Europa's UV absorption band. *Nature* **292**, 38–39.

Lanzerotti, L. J., W. L. Brown, J. M. Poate, and W. M. Augustyniak 1978. On the contribution of water products from Galilean satellites to the jovian magnetosphere. *Geophys, Res. Lett.* **5**, 155–158.

Lean, J. 1997. The Sun's variable radiation and its relevance for Earth. *Annu. Rev. Astron. Astrophys.* **35**, 33–67.

Lean, J. D., G. J. Rottman, H. L. Kyle, T. N. Woods, J. R. Hickey, and L. C. Puga 1997. Detection and parameterization of variations in solar mid- and near-ultraviolet radiation (200–400 nm). *J. Geophys. Res.* **102**, 29939–29956.

Lefort, M. 1955. Chimie des Radiations des solutions aqueuses, chapter II. In *Actions Chiniques et Bilogiques des Radiations Vol. 1* (M. Haissinsky, Ed.), p. 203. Masson, Paris.

Mauk, B. H., S. A. Gary, M. Kane, E. P. Keath, and S. M. Krimigis 1996. Hot plasma parameters of Jupiter's inner magnetosphere. *J. Geophys. Res.* **101**, 7685–7695.

Mauk, B. H., D. J. Williams, and R. W. McEntire 1997. Energy-time dispersed charged particle signatures of dynamic injections in Jupiter's inner magnetosphere. *Geophys. Res. Lett.* **24**, 2949–2952.

Mauk, B. H., D. J. Williams, R. W. McEntire, K. K. Khurana, and J. G. Roederer 1999. Storm-like dynamics of Jupiter's inner and middle magnetosphere. *J. Geophys. Res.* **104**, 22759–22778.

McCord, T. B., and 12 colleagues 1997. Organics and other molecules in the surfaces of Callisto and Ganymede. *Science* **278**, 271–275.

McCord, T. B., and 11 colleagues 1998a. Salts on Europa's surface detected by Galileo's Near Infrared Mapping Spectrometer. *Science* **280**, 1242–1245.

McCord, T. B., and 12 colleagues 1998b. Non-water-ice constituents in the surface material of the icy Galilean satellites from the Galileo near-infrared mapping spectrometer investigation. *J. Geophys. Res.* **103**, 8603–8626.

McCord, T. B., and 11 colleagues 1999. Hydrated salt minerals on Europa's surface from the Galileo near-infrared mapping spectrometer (NIMS) investigation. *J. Geophys. Res.* **104**, 11827–11851.

McIlwain, C. E. 1966. Magnetic coordinates. *Space Sci. Rev.* **5**, 585–598.

McKinnon, W. B. 1999. Convective instability in Europa's floating ice shell. *Geophys. Res. Lett.* **26**, 951–954.

Miller, S. L. 1953. A production of amino acids under possible primitive Earth conditions. *Science* **117**, 528–529.

Miller, S. L. 1969. Clathrate hydrates of air in Antarctic ice. *Science* **165**, 489–490.

Miller, S. L., and J. L. Bada 1988. Submarine hot springs and the origin of life. *Nature* **334**, 609–611.

Moore, M. H., and B. Donn 1982. The infrared spectrum of a laboratory-synthesized residue: Implications for the 3.4-μm interstellar absorption feature. *Astrophys. J.* **257**, L47–L50.

Moore, M. H., and R. L. Hudson 2000. IR detection of H_2O_2 at 80 K in ion-irradiated laboratory ices relevant to Europa. *Icarus* **145**, 282–288.

Moore, M. H., and R. K. Khanna 1991. Infrared and mass spectral studies of proton irradiated $H_2O + CO_2$ ice: Evidence for carbonic acid. *Spectrochim. Acta* **47A**, 255–262.

Moore, M. H., B. Donn, R. Khanna, and M. F. A'Hearn 1983. Studies of proton-irradiated cometary-type ice mixtures. *Icarus* **54**, 388–405.

Moore, M. H., R. F. Ferrante, and J. A. Nuth III 1996. Infrared spectra of proton irradiated ices containing methanol. *Plan. Sp. Sci.* **44**, 927–935.

Moore, M. H., R. Khanna, and B. Donn 1991. Studies of proton irradiated $H_2O + CO_2$ and $H_2O + CO$ ices and analysis of synthesized molecules. *J. Geophys. Res.* **96**, 17541–17545.

Moore, J. M., and 13 colleagues 1999. Mass movement and landform degradation on the icy Galilean satellites: Results from the Galileo nominal mission. *Icarus* **140**, 294–312.

Morris, R. V. 1978. In situ reworking (gardening) of the lunar surface: Evidence from the Apollo cores. *Geochim. Cosmochim. Acta* **2**, 1801–1811.

Nelson, R. M., A. L. Lane, D. L. Matson, G. J. Veeder, B. J. Buratti, and E. F. Tedesco 1987. Spectral geometric albedos of the galilean satellites from 0.24 to 0.34 micrometers: Observations with the International Ultraviolet Explorer. *Icarus* **72**, 358–380.

Neukum, G. 1997. Bombardment history of the jovian system. In *The Three Galileos: The Man, The Spacecraft, The Telescope* (C. Barbieri *et al.*, Eds.), pp. 201–212. Kluwer Academic, the Netherlands.

Noll, K. S., R. E. Johnson, A. L. Lane, D. L. Domingue, and H. L. Weaver 1996. Detection of ozone on Ganymede. *Science* **273**, 341–343.

Noll, K. S., R. E. Johnson, M. A. McGrath, and J. J. Caldwell 1997a. Detection of SO_2 on Callisto with the Hubble Space Telescope. *Geophys. Res. Lett.* **24**, 1139–1142.

Noll, K. S., T. L. Roush, D. P. Cruikshank, R. E. Johnson, and Y. J. Pendleton 1997b. Detection of ozone on Saturn's satellites Rhea and Dione. *Nature* **388**, 45–47.

Ockert-Bell, M. E., J. A. Burns, I. J. Daubar, P. C. Thomas, and J. Veverka 1998. The structure of Jupiter's ring system as revealed by the Galileo imaging experiment. *Icarus* **138**, 188–213.

Öpik, E. J. 1951. Collision probabilities with the planets and the distribution of interplanetary matter. *Proc. R. Irish Acad.* **54**, 165–199.

Orlando, T. M., and G. A. Kimmel 1997. The role of excitons and the substrate temperature in low-energy (5–50 eV) electron-stimulated dissociation of amorphous D_2O ice. *Surf. Sci.* **390**, 79–85.

Paonessa, M. T., and A. F. Cheng 1985. A theory of satellite sweeping. *J. Geophys. Res.* **90**, 3428–3434.

Pappalardo, R. T., J. W. Head, R. Greeley, R. J. Sullivan, C. Pilcher, G. Schubert, W. B. Moore, M. H. Carr, J. M. Moore, and M. J. S. Belton 1998. Geological evidence for solid-state convection in Europa's ice shell. *Nature* **391**, 365–368.

Paranicas, C., A. F. Cheng, and D. J. Williams 1998. Inference of Europa's conductance from the Galileo Energetic Particles Detector. *J. Geophys. Res.* **103**, 15001–15007.

Paranicas, C., W. R. Paterson, A. F. Cheng, B. H. Mauk, R. W., McEntire, L. A. Frank, and D. J. Williams 1999. Energetic particle observations near Ganymede. *J. Geophys. Res.* **104**, 17459–17469.

Passey, Q. R., and E. M. Shoemaker 1982. 12. Craters and basins on Ganymede and Callisto: Morphological indicators of crustal evolution. In *The Satellites of Jupiter* (D. Morrison, Ed.), pp. 379–434. Univ. of Arizona Press, Tucson.

Pospieszalska, M. K., and R. E. Johnson 1989. Magnetospheric ion bombardment profiles of satellites: Europa and Dione. *Icarus* **78**, 1–13.

Purves, N. G., and C. B. Pilcher 1980. Thermal migration of water on the Galilean satellites. *Icarus* **43**, 51–55.

Sauer, H. H., and E. C. Ray 1963. On cosmic ray cutoffs. *Ann. Phys.* **25**, 135–142.

Sauer, J., D. F. Strobel, and F. M. Neubauer 1998. Interaction of the jovian magnetosphere with Europa: Constraints on the neutral atmosphere. *J. Geophys. Res.* **103**, 19947–19962.

Schlesinger, W. H. 1997. *Biogeochemistry: An Analysis of Global Change*, p. 302. Academic Press, San Diego.

Shaya, E. J., and C. B. Pilcher 1984. Polar cap formation on Ganymede. *Icarus* **58**, 74–80.

Shea, M. A., D. F. Smart, and H. Carmichael 1976. *Summary of Cutoff Rigidities Calculated with the International Geomagnetic Reference Field for Various Epochs.* Air Force Geophysics Laboratory, AFGL-TR-76-0115.

Shi, M., R. A. Baragiola, D. E. Grosjean, R. E. Johnson, S. Jurac, and J. Schou 1995. Sputtering of water ice surfaces and the production of extended neutral atmospheres. *J. Geophys. Res.* **100**, 26387–26395.

Shoemaker, E. M., and R. F. Wolfe 1982. 10. Cratering time scales for the Galilean satellites. In *The Satellites of Jupiter* (D. Morrison, Ed.), pp. 277–339. Univ. of Arizona Press, Tucson.

Shoemaker, E. M., B. K. Lucchitta, D. E. Wilhems, J. B. Plescia, and S. W. Squyres 1982. 13. The Geology of Ganymede. In *The Satellites of Jupiter* (D. Morrison, Ed.), pp. 435–520. Univ. of Arizona Press, Tucson.

Showman, A. P., and R. Malhotra 1997. Tidal evolution into the Laplace resonance and the resurfacing of Ganymede. *Icarus* **127**, 93–111.

Showman, A. P., and R. Malhotra 1999. The Galilean satellites. *Science* **286**, 77–84.

Showman, A. P., D. J. Stevenson, and R. Malhotra 1997. Coupled orbital and thermal evolution of Ganymede. *Icarus* **129**, 367–383.

Sieger, M. T., W. C. Simpson, and T. M. Orlando 1998. Production of O_2 on icy surfaces by electronic excitation of low-temperature water ice. *Nature* **394**, 554–556.

Sieveka, E. M., and R. E. Johnson 1982. Thermal- and plasma-induced molecular redistribution on the icy satellites. *Icarus* **51**, 528–548.

Smart, D. F., and M. A. Shea 1967. A study of the effectiveness of the McIlwain coordinates in estimating cosmic-ray vertical cutoff rigidities. *J. Geophys. Res.* **72**, 3447–3454.

Smart, D. F., and M. A. Shea 1973. An empirical method of estimating cutoff rigidities at satellite altitudes. In *Proceedings, 13th International Cosmic Ray Conference, Denver*, Vol. 2, pp. 1070–1074, University of Denver, Denver.

Spaun, N. A., J. W. Head, G. C. Collins, L. M. Prockter, and R. T. Pappalardo 1998. Conamara chaos region, Europa: Reconstruction of mobile polygonal blocks. *Geophys. Res. Lett.* **25**, 4277–4280.

Spencer, J. R. 1987a. Thermal segregation of water ice on the Galilean satellites. *Icarus* **69**, 297–313.

Spencer, J. R. 1987b. Icy Galilean satellite reflectance spectra—Less ice on Ganymede and Callisto? *Icarus* **70**, 99–110.

Spencer, J. 1998. Upper limits for condensed O_2 on Saturn's icy satellites and rings. *Icarus* **136**, 349–352.

Spencer, J. R., W. M. Calvin, and M. J. Person 1995. Charged-coupled device spectra of the Galilean satellites: Molecular oxygen on Ganymede. *J. Geophys. Res.* **100**, 19049–19056.

Spencer, J. R., L. K. Tamppari, T. Z. Martin, and L. D. Travis 1999. Temperatures on Europa from Galileo photopolarimeter-radiometer: Nighttime thermal anomalies. *Science* **284**, 1514–1516.

Squyres, S. W., R. T. Reynolds, P. M. Cassen, and S. J. Peale 1983. Liquid water and active resurfacing on Europa. *Nature* **301**, 225–226.

Stone, E. C. 1963. The physical significance and application of L, B_0, and R_0 to geomagnetically trapped particles. *J. Geophys. Res.* **68**, 4157–4166.

Størmer, C. 1955. *The Polar Aurora*. Oxford University Press, Oxford.

Strazzulla, G., and R. E. Johnson 1991. Irradiation effects on comets and cometary debris. In *Comets in the Post-Halley Era* (R. L. Newburn, Jr., M. Neugebauer, and J. Rahe, Eds.), Vol. 1 pp. 243–275. Kluwer-Academic, the Netherlands.

Strazzulla, G., and M. E. Palumbo 1998. Evolution of icy surfaces: An experimental approach. *Plan. Sp. Sci.* **46**, 1339–1348.

Sullivan, R., *et al.* 1998. Episodic plate separation and fracture infill on the surface of Europa. *Nature* **391**, 371–373.

Vasyliunas, V. M. 1971. Deep space plasma measurements. In *Methods of Experimental Physics* (R. H. Loveberg and H. R. Griem, Eds.), **9B**, p. 49, Academic Press, San Diego.

Vidal, R. A., D. Bahr, R. A. Baragiola, and M. Peters 1997. Oxygen on Ganymede: Laboratory studies. *Science* **276**, 1839–1842.

Volwerk, M., M. G. Kivelson, K. K. Khurana, and R. L. McPherron 1999. Probing Ganymede's magnetosphere with field line resonances. *J. Geophys. Res.* **104**, 14729–14738.

Warren, S. G. 1984. Optical constants of ice from the ultraviolet to the microwave. *Appl. Opt.* **23**, 1206–1225.

Williams, D. J., and 10 colleagues 1997a. Energetic particle signatures at Ganymede: Implications for Ganymede's magnetic field. *Geophys. Res. Lett.* **24**, 2163–2166.

Williams, D. J., B. Mauk, R. W. McEntire 1997b. Trapped electrons in Ganymede's magnetic field. *Geophys. Res. Lett.* **24**, 2953–2956.

Williams, D. J., B. Mauk, and R. W. McEntire 1998. Properties of Ganymede's magnetosphere as revealed by energetic particle observations. *J. Geophys. Res.* **103**, 17523–17534.

Williams, D. J., R. W. McEntire, S. Jaskulek, and B. Wilken 1992. The Galileo Energetic Particles Detector. *Sp. Sci. Rev.* **60**, 385–412.

Williams, K. K., and R. Greeley 1998. Estimates of ice thickness in the Conamara chaos region of Europa. *Geophys. Res. Lett.* **25**, 4273–4276.

Woon, D. E. 1999. Ab initio quantum chemical studies of reactions in astrophysical ices 1. Aminolysis, hydrolysis, and polymerization in $H_2CO/NH_3/H_2O$ ices. *Icarus* **142**, 550–556.

Zahnle, K., L. Dones, and H. F. Levison 1998. Cratering rates on the Galilean satellites. *Icarus* **136**, 202–222.

Ziegler, J. F., J. P. Biersack, and U. Littmark 1985. *The Stopping and Range of Ions in Solids*. Pergamon Press, New York.